Research Square

Preprints are preliminary reports that have not undergone peer review.
They should not be considered conclusive, used to inform clinical practice,
or referenced by the media as validated information.

Pinning-Controlled Reaction–Diffusion–Advection Dynamics of Iron Band Formation in Zebra Rocks

Biswajit Saha

biswajitsaha.1987.bs@gmail.com

Gobardanga Hindu College

Manas Kumar Roy

Brahmananda Keshab Chandra College

Research Article

Keywords: Zebra rock, Pattern formation, Reaction–diffusion–advection, Iron oxide precipitation, Self-organization, Pinning effect, Liesegang banding

Posted Date: October 26th, 2026

DOI: https://doi.org/10.21203/rs.3.rs-11088572/v1

License: This work is licensed under a Creative Commons Attribution 4.0 International License.
Read Full License

Additional Declarations: No competing interests reported.

Pinning-Controlled Reaction–Diffusion–Advection Dynamics of Iron Band Formation in Zebra Rocks

Biswajit Saha[1*] and Manas Kumar Roy[2]

[1*]Department of Physics, Gobardanga Hindu College, Gobardanga, 743273, West Bengal, India.
[2]Department of Physics, Brahmananda Keshab Chandra College, 111/2 B.T. Road, Bonhooghly, Kolkata, 700108, West Bengal, India.

*Corresponding author(s). E-mail(s): biswajitsaha.1987.bs@gmail.com;
Contributing authors: manask.roy@gmail.com;

Abstract

Zebra rocks from East Kimberley exhibit rhythmic hematite banding with spacings of 0.5–2.0 mm. We test whether this pattern arises from self-organization during hydrothermal alteration using a reaction–transport model coupling Darcy flow, diffusion, and nonlinear precipitation kinetics. Following the continuum-phase approach of Baruah et al. (2023), we treat the felsic (Fe^{2+}-bearing fluid) and mafic (Fe^{3+}-precipitate) constituents as two petrologically interacting continuum phases. Linear stability analysis reveals that the system exhibits a saddle-focus instability ($\mathbf{Tr(J) = 0.023 > 0}$, $\mathbf{det(J) \approx 0}$) rather than a pure Turing instability; pattern formation is driven by nonlinear reaction kinetics and advective transport. Host-rock heterogeneities—represented as pinning sites following the pinning field concept of Baruah et al. (2023)—provide the localized perturbations ($\boldsymbol{\eta = 10^{-4}}$) that break spatial symmetry. Two-dimensional simulations reproduce key field characteristics with mean spacing of 1.45 mm, dominant wavelength of 1.25 mm, pattern contrast of 0.986, CV = 3.8%, and Liesegang coefficient $\boldsymbol{p = 1.001 \pm 0.056}$, all consistent with natural observations. The 95% confidence interval ($\boldsymbol{p \in [0.891, 1.112]}$) includes $\boldsymbol{p = 1.0}$, confirming nearly constant band spacing in the advection-dominated regime ($\boldsymbol{v \approx 6.36 \times 10^{-6}}$ m/s). The four interface pattern types recognized by Baruah et al. (2023)—planar, wavy, fingering, and incoherent—are shown to emerge naturally from our model under varying diffusion coefficients, pinning strengths, and reaction coupling. This study provides a quantitative framework linking millimetre-scale mineral textures to self-organized hydrothermal processes, with pinning heterogeneities providing the symmetry-breaking mechanism for pattern initiation.

Keywords: Zebra rock; Pattern formation; Reaction–diffusion–advection; Iron oxide precipitation; Self-organization; Pinning effect; Liesegang banding

PAC Codes: 47.54.-r , 47.27.te , 91.60.-x , 05.45.-a

Highlights

- Zebra-rock banding emerges under saddle-focus instability conditions ($\mathrm{Tr}(\mathbf{J}) = 0.023 > 0$, $\det(\mathbf{J}) \approx 0$) with strong differential diffusion ($D_{Fe^{2+}}/D_{Fe^{3+}} = 4.0$).
- Advective Darcy flow ($v \approx 6.36 \times 10^{-6}$ m s^{-1}) controls band orientation and breaks isotropic symmetry.
- Numerical simulations reproduce natural zebra-rock spacings, yielding a mean band spacing of 1.45 mm and dominant wavelength of 1.25 mm within the observed field range of 0.5–2.0 mm.
- Highly regular banding arises from nonlinear autocatalytic precipitation, with low spacing variability (CV = 3.8%) and pattern contrast of 0.986.
- Liesegang-type spacing behaviour ($p = 1.001 \pm 0.056$) emerges naturally from reaction–transport coupling; 95% CI ($p \in [0.891, 1.112]$) includes $p = 1.0$, confirming constant spacing.
- Host-rock pinning heterogeneities ($\eta = 10^{-4}$) act as symmetry-breaking nucleation sites that trigger pattern formation, providing a physically realistic alternative to arbitrary random noise for pattern initiation.

- The four interface pattern types of Baruah et al. (2023)—planar, wavy, fingering, and incoherent—emerge naturally from our model under varying diffusion coefficients, pinning strengths, and reaction coupling.

1 Introduction

1.1 Geological Significance of Zebra Rocks

Rhythmic foliation patterns, often termed *zebra textures* or *zebra rocks*, rank among the most visually striking and scientifically intriguing structures in geology. Characterized by alternating dark and light bands with thicknesses ranging from millimetres to several centimetres, these patterns manifest in diverse lithologies including dolostones, claystones, and siderite-rich rocks Loughnan and Roberts (1990); Wallace et al. (1994); Palinkaš et al. (2009); Merino and Canals (2011). First described in detail from the East Kimberley region of Western Australia Loughnan and Roberts (1990), the archetypal 'zebra rock' presents a dramatic pattern of rhythmic, red to purple iron-oxide bands set within a pale, kaolinitic siltstone matrix, a contrast that has rendered it a notable decorative stone and a subject of enduring geological inquiry Pillans (2021).

The economic and scientific importance of understanding zebra rock formation extends beyond academic curiosity. These rocks serve as natural archives of palaeo-fluid flow, chemical conditions, and diagenetic history. Moreover, similar banded textures in other geological settings may provide insights into ore deposit formation, hydrocarbon migration pathways, and palaeoenvironmental reconstruction. The East Kimberley zebra rock, with its exceptional preservation and accessibility, provides an ideal natural laboratory for studying self-organized pattern formation in geological systems.

1.2 Historical Perspective on Pattern Formation Mechanisms

The genesis of these enigmatic patterns has been a fertile ground for scientific debate, giving rise to two broad, often complementary, schools of thought. Traditional models emphasize structural and diagenetic processes. In these views, zebra textures are essentially *templated* by pre-existing heterogeneities or cyclic events. Processes such as tectonic or hydrofracturing create void networks that are subsequently filled by coarse crystalline cement, leading to banding Wallace et al. (1994); Newman and Mitra (1994). Syn-sedimentary or early diagenetic rhythms, potentially linked to evaporite dissolution and collapse brecciation, can also provide an initial architecture for later mineral infill Karakitsios and Pomoni-Papaioannou (1998); Tompkins et al. (1994).

However, the remarkable symmetry, periodicity, and grain-size contrast inherent in many zebra textures have long hinted at a more intrinsic, dynamic origin. This has led to the second major framework: *self-organization*. Self-organization refers to the spontaneous emergence of ordered spatial or temporal patterns in systems driven far from thermodynamic equilibrium, regulated by internal nonlinear feedback loops between reaction, transport, and sometimes mechanical processes Karsenti (2008); Taylor and Tinsley (2009); Ortoleva (1984); Ortoleva et al. (1987). For zebra textures, self-organization models posit that the banding is not an imprint of an external template but an innate, dynamical consequence of the geochemical system's evolution.

1.3 The East Kimberley Zebra Rock: A Case Study

The zebra rock of the East Kimberley provides a compelling and focused case study at the intersection of these paradigms. Recent high-resolution mineralogical and geochemical work strongly favors a self-organized, Liesegang-type mechanism within a hydrothermal context Abrajevitch et al. (2018); Kawahara et al. (2022); Coward et al. (2023). The model proposes infiltration of an acidic, reducing, iron-bearing fluid into a permeable siliciclastic sediment. As this fluid migrates, it is neutralized by reaction with primary carbonate or silicate minerals, causing a progressive increase in pH. This pH change triggers the oxidation and precipitation of iron (initially present as Fe^{2+}) as Fe-oxyhydroxides (e.g., hematite), forming the distinctive red bands.

Recent theoretical advances have further demonstrated the utility of reaction-diffusion models for understanding metamorphic textures. Saha and Roy Saha and Roy (2026) developed a fractional Gierer-Meinhardt model that successfully reproduces complex pattern formation in metamorphic rocks, while Saha et al. Saha et al. (2025) showed that diffusion-driven dynamics can explain orbicular textures in metamorphic granites. These studies provide a foundation for extending reaction-diffusion frameworks to the specific case of zebra rock banding.

1.4 Continuum-Phase Approach and Pinning Effects

A powerful framework for understanding pattern formation in geological systems has been developed by Baruah et al. Baruah et al. (2023), who modeled petrological mixing mechanisms in the evolution of continental crusts using a Turing-type reaction-diffusion (RD) approach. Their work treats petrologically interacting phases—felsic (F) and mafic (M) constituents—as two continuum phases, where the diffusion coefficient assigned to each phase represents the bulk diffusion properties of the participating rocks, constituted by diverse minerals with

different diffusional properties DePaolo and Getty (1996); Watson and Baxter (2007). This continuum-phase approach is fundamentally applicable to two coexisting phases with a chemically interactive relationship, where one phase invades into the other through phase boundary migration.

Baruah et al. Baruah et al. (2023) introduced the concept of a *pinning field* (W) to represent microscale heterogeneities that introduce disordering in the mass transport process. In natural geological systems, heterogeneities in porosity, permeability, mineral grain distribution, or pre-existing fractures provide localized perturbations that break spatial symmetry and initiate instability. The reaction between the two participating phases must overcome the pinning threshold at specific particle locations in space and time. This pinning concept is particularly relevant to zebra rock formation, where host-rock heterogeneities act as nucleation sites for rhythmic precipitation.

The Baruah et al. Baruah et al. (2023) study recognized four types of interface patterns between interacting phases: (i) **Type I (planar)**—nearly planar first-order geometry with locally low-amplitude irregularities, forming when diffusion coefficients are equal and pinning is absent; (ii) **Type II (wavy)**—multi-ordered irregular geometry with power-law distributions, forming under lower diffusion coefficients; (iii) **Type III (fingering)**—finger-like incursion of one phase into the other, forming under contrasting diffusion coefficients and strong pinning; and (iv) **Type IV (incoherent)**—isolated or partially connected masses of one phase hosted in the other, forming under nonlinear reaction coupling and pinning. These four pattern types provide a natural classification scheme for the banding patterns observed in zebra rocks.

1.5 Experimental Evidence and Modeling Motivation

Recent experimental advances have provided direct evidence for such self-organized precipitation mechanisms. In a landmark study, Yatsuda et al. (2023) used chemical experiments and numerical simulations to reproduce the periodic precipitation of iron oxide minerals in a gel medium. By diffusing NaOH into a gel containing ferrous ions, they observed the periodic precipitation of $Fe(OH)_2$ via a Liesegang-type mechanism, as confirmed by the spacing law and Matalon–Packter law. Subsequent aerobic oxidation converted the $Fe(OH)_2$ pattern into FeOOH without altering the periodic banding, with further high-temperature oxidation expected to yield Fe_2O_3 (hematite) patterns. Their reaction–diffusion simulations, which considered a continuous flux of ferrous ions into the reaction field, successfully reproduced the observed periodic patterns. While this work provides crucial experimental validation for the Liesegang mechanism of iron oxide band formation, it was conducted in idealized gel media rather than porous rock matrices and did not incorporate the advective transport that characterizes natural hydrothermal systems. Our study extends this framework by incorporating Darcy-scale fluid flow and applying it to the specific geological context of the East Kimberley zebra rock.

A critical aspect often overlooked in deterministic models is the role of initial perturbations or "pinning effects" in triggering pattern formation. In natural geological systems, heterogeneities in porosity, permeability, mineral grain distribution, or pre-existing fractures provide the localized perturbations necessary to break spatial symmetry and initiate instability Chadam et al. (1986); Ortoleva et al. (1987). Unlike random noise, which assumes arbitrary perturbations, the pinning effect represents physically realistic heterogeneities in the host rock that act as nucleation sites for pattern formation. In our model, we incorporate Gaussian white noise of amplitude $\eta = 10^{-4}$ as an initial perturbation, representing the natural heterogeneities (pinning sites) present in sedimentary rocks. These pinning sites seed pattern formation and determine the spatial phase of the emerging bands, providing a more geologically realistic mechanism for pattern initiation than arbitrary noise. This approach follows the pinning field concept of Baruah et al. Baruah et al. (2023), who demonstrated that pinning heterogeneities are essential for triggering pattern formation in geological systems.

1.6 Research Objectives and Approach

Despite recent progress, a quantitative, process-based model that captures the essential physics and chemistry of iron-redox-driven banding in porous geological media has been lacking. We construct a modified Gray–Scott-type reaction-diffusion model Gray and Scott (1984); Amin and Mashat (2021); Buric (2014), a canonical framework for studying pattern formation in nonlinear chemical systems. This framework is strategically augmented to encapsulate the key processes relevant to zebra rock formation: (1) Advective transport via Darcy flow, representing the pressure-driven infiltration of the hydrothermal fluid through the sedimentary host; (2) Nonlinear autocatalytic kinetics adapted to represent the redox interplay between ferrous (Fe^{2+}) and ferric (Fe^{3+}) iron; (3) Anisotropic initial and boundary conditions to reflect the lithological layering or structural fabric that guides the preferential orientation of bands; and (4) Pinning perturbations representing host-rock heterogeneities that trigger pattern formation and determine pattern phase, following the pinning field concept of Baruah et al. Baruah et al. (2023). Our approach builds upon but significantly extends the work of Yatsuda et al. (2023) by: (i) incorporating advective transport relevant to hydrothermal systems, (ii) using geologically realistic parameters derived from East Kimberley field data, (iii) simulating pattern formation in a

porous matrix rather than a gel medium, (iv) providing quantitative comparison with natural zebra rock metrics including band spacing, regularity, and Liesegang coefficients, (v) explicitly modeling the role of pinning heterogeneities in triggering pattern formation, and (vi) demonstrating that the four interface pattern types of Baruah et al. Baruah et al. (2023) emerge naturally from our model under varying diffusion coefficients, pinning strengths, and reaction coupling.

2 Stress-Induced Foliation vs. Chemically-Driven Banding in Metamorphic Rocks

2.1 Fundamentals of Metamorphic Foliation

Foliation is a fundamental planar fabric element pervasive in deformed metamorphic rocks, classically defined by the parallel alignment of platy or elongate mineral grains such as micas and amphiboles. This alignment is a direct textural response to the application of differential stress during regional metamorphism, combined with temperature-driven recrystallization Passchier and Trouw (2005); Vernon (2004). The canonical sequence for the development of such tectonometamorphic foliation begins with the burial and heating of an original layered protolith (characterized by primary sedimentary or volcanic bedding, termed S_0). Subsequent directed stress induces mechanical rotation and/or dissolution of minerals, while concomitant recrystallization fosters the growth of new minerals with a preferred orientation perpendicular to the maximum compressive stress, forming a penetrative foliation plane (S_1) Spear (1993). In high-grade metamorphism, this process can be accompanied by metamorphic differentiation, where chemical migration via diffusion or pressure solution leads to the segregation of minerals into distinct compositional bands, producing gneissic textures Bhattacharya (2022).

2.2 Distinguishing Chemical from Mechanical Banding

However, a critical distinction must be drawn between this stress-induced, mechanically dominated foliation and rhythmic compositional banding of the type exemplified by the zebra rock of the East Kimberley. While both can produce visually striking planar fabrics, their underlying formation mechanisms are fundamentally different. Stress-induced foliation requires sustained differential stress to align grains. In contrast, banding in zebra textures—and in many other mineralized carbonate and siliciclastic systems—displays a periodicity, symmetry, and microstructural character that suggest an origin governed by nonlinear geochemical feedbacks under fluid-rich conditions, often with minimal or no direct mechanical forcing Merino and Canals (2011); Kelka et al. (2015). These are best understood as self-organized patterns, where the regular alternation of mineralogy and texture emerges spontaneously from the internal dynamics of the reacting fluid-rock system, driven far from equilibrium Ortoleva (1984); Ortoleva et al. (1987); Karsenti (2008).

2.3 The Zebra Rock Paradigm

The zebra rock provides a paradigm for this dichotomy. Its exquisite, rhythmically spaced iron-oxide bands within a kaolinitic matrix Loughnan and Roberts (1990); Abrajevitch et al. (2018) lack the penetrative grain alignment indicative of strong directed stress. Instead, mineralogical and geochemical evidence points to an *isochemical to metasomatic origin via fluid infiltration*. Recent studies conclude the banding formed from the infiltration of an acidic, Fe^{2+}-bearing hydrothermal fluid into a permeable sedimentary unit. The rhythmic precipitation of hematite is interpreted as a *Liesegang-type phenomenon*, where patterns arise from coupled reaction and diffusion (or advection) processes, not from mechanical deformation Kawahara et al. (2022); Coward et al. (2023); Yoshida et al. (2020). This places its genesis firmly within the realm of *reaction-transport self-organization*, a process distinct from, and potentially independent of, tectonic foliation development.

Therefore, while the classic model of foliation development—encompassing stages from burial (S_0 preservation) through stress application, recrystallization, and possible differentiation to form gneissic banding—explains a vast array of regionally metamorphosed rocks, it is an insufficient model for rhythmic, chemical banding like that of the zebra rock. The latter necessitates a different conceptual framework, one that prioritizes *fluid-mediated chemical kinetics, solute transport, and nonlinear feedback* over differential stress and mechanical rotation. We explicitly model the zebra rock's banding not as a tectonic foliation but as a *purely geochemical pattern* emerging from the interplay of fluid flow, diffusion, and redox reactions. The successful simulation of periodic banding through such a model reinforces the principle that not all planar fabrics in rocks are foliations in the tectonic sense; some are the fossilized signatures of ancient reaction-diffusion-advection systems.

3 Geochemical Self-Organization and Iron Banding in Zebra Rock

3.1 Overview of Formation Mechanisms

The distinctive rhythmic banding of the East Kimberley zebra rock—characterized by alternating red-brown (hematite-rich) and light (kaolinite/quartz-rich) layers—has been the subject of varied genetic hypotheses. Early models proposed diagenetic processes like pyrite oxidation and colloidal coagulation under fluctuating pH conditions Loughnan and Roberts (1990). More recently, a pedogenic (soil-forming) model involving microbial iron cycling in Ediacaran paleosols has been suggested Retallack (2021). However, these models struggle to explain the high degree of spatial regularity, lateral continuity, and sharp mineralogical zoning observed in the banding. An alternative, increasingly supported framework invokes *geochemical self-organization* via a Liesegang-type periodic precipitation mechanism Sadek and Sultan (2011); Nakouzi and Steinbock (2016). In this view, an infiltrating, iron-bearing fluid interacts with a reactive host rock, with rhythmic iron-oxide precipitation arising spontaneously from nonlinear feedback between advection, diffusion, reaction kinetics, and local supersaturation. This framework provides a robust, process-based explanation for both the macroscopic banding and the associated microscale geochemical heterogeneity.

3.2 Geological Context and Acidic Hydrothermal Alteration

Zebra rock occurs within the Johnny Cake Shale Member of the Ranford Formation in the East Kimberley region of Western Australia. The host rock is a fine-grained, feldspathic to micaceous lacustrine (lake-deposited) siltstone of Neoproterozoic age Abrajevitch et al. (2018). Mineralogical and geochemical evidence strongly points to alteration by an acidic, sulfate-rich, and Fe^{2+}-bearing hydrothermal fluid Kawahara et al. (2022); Coward et al. (2023). This event led to *advanced argillic alteration*, a mineral assemblage indicative of low-pH (pH < 5) and oxidizing conditions, with estimated temperatures exceeding 120°C. Key mineral transformation reactions during this event include:

- **Feldspar alteration to alunite:**

$$3KAlSi_3O_8 + 18H_2O + 2SO_4^{2-} + 6H^+ \rightarrow KAl_3(SO_4)_2(OH)_6 + 9H_4SiO_4 + 2K^+ \tag{1}$$

- **Muscovite alteration:**

$$KAl_2(Si_3Al)O_{10}(OH)_2 + 6H_2O + 2SO_4^{2-} + 4H^+ \rightarrow KAl_3(SO_4)_2(OH)_6 + 3H_4SiO_4 \tag{2}$$

- **Kaolinite formation:**

$$2KAlSi_3O_8 + 9H_2O + 2H^+ \rightarrow Al_2Si_2O_5(OH)_4 + 4H_4SiO_4 + 2K^+ \tag{3}$$

These reactions produced the characteristic mineralogy of the light bands: kaolinite, dickite, and locally alunite, while simultaneously releasing silica (as aqueous H_4SiO_4) and cations (K^+) to the fluid.

3.3 Mechanism of Rhythmic Iron-Oxide Band Formation

The key to pattern formation lies in the coupled behaviour of iron and hydrogen ions. The infiltrating hydrothermal fluid is acidic and carries reduced iron (Fe^{2+}). Rhythmic banding emerges from a feedback loop between iron oxidation/precipitation and pH buffering by the silicate host rock:

1. **Fluid Infiltration and Oxidation:** Fe^{2+} is transported by advective flow. Upon encountering oxidising conditions, it oxidises:
$$4Fe^{2+} + O_2 + 4H^+ \rightarrow 4Fe^{3+} + 2H_2O \tag{4}$$
2. **Precipitation Trigger:** The produced Fe^{3+} is highly insoluble and hydrolyses to form amorphous $Fe(OH)_3$ (aging to hematite, Fe_2O_3):
$$Fe^{3+} + 3H_2O \rightarrow Fe(OH)_3 \downarrow + 3H^+ \tag{5}$$
Critically, this precipitation reaction *re-acidifies* the local environment.
3. **pH Buffering and Feedback:** The newly generated acid is neutralised (buffered) by the ongoing dissolution of primary aluminosilicate minerals (e.g., feldspar). This buffering reaction consumes H^+ and releases aqueous species, but also causes a local *increase in pH*. This pH rise pushes the system back towards conditions favouring Fe^{3+} precipitation, creating a new precipitation front slightly ahead of the previous one.

This cycle of *precipitation-acidification-buffering-re-precipitation* repeats, generating a periodic sequence of iron-oxide bands. The spacing is controlled by the relative rates of fluid flow, diffusion of H^+ and Fe^{2+}, and the kinetics of the dissolution and precipitation reactions Yoshida et al. (2020).

3.4 Pinning Effect and Pattern Initiation

A critical component of our model is the incorporation of pinning sites to trigger pattern formation, following the pinning field concept of Baruah et al. Baruah et al. (2023). In natural geological systems, heterogeneities in the host rock—such as variations in porosity, permeability, mineral composition, or pre-existing fractures—provide localized nucleation sites that break the spatial symmetry of the system. These heterogeneities act as "pinning centers" that determine the phase and spatial distribution of the emerging patterns.

The initial conditions are defined as:

$$u(\mathbf{x}, 0) = u_0(\mathbf{x}) + \eta\xi_p(\mathbf{x}), \quad v(\mathbf{x}, 0) = v_0(\mathbf{x}) + \eta\xi_p(\mathbf{x}) \tag{6}$$

where $u_0(\mathbf{x}) = 1 - e^{-80(y+0.05)}$ and $v_0(\mathbf{x}) = e^{-80y}$ represent the deterministic concentration profiles, $\eta = 10^{-4}$ is the pinning strength amplitude, and $\xi_p(\mathbf{x})$ is a spatial perturbation field representing host-rock heterogeneities (e.g., porosity variations, mineral grain boundaries, or fracture networks).

The pinning effect differs fundamentally from arbitrary random noise in several important ways:

1. **Physical Realism:** Pinning sites correspond to actual geological heterogeneities (pore structure, mineral grains, fractures), whereas random noise is an artificial construct.
2. **Spatial Correlation:** Natural heterogeneities often exhibit spatial correlation (e.g., bedding-parallel porosity variations), unlike uncorrelated white noise.
3. **Pattern Control:** Pinning sites provide deterministic control over pattern phase and nucleation locations, leading to more reproducible patterns.
4. **Geological Justification:** The pinning effect is consistent with Liesegang banding theory, where heterogeneities in the medium act as nucleation sites for periodic precipitation Sadek and Sultan (2011); Nakouzi and Steinbock (2016), and with the pinning field concept of Baruah et al. Baruah et al. (2023), who demonstrated that pinning heterogeneities are essential for triggering pattern formation in geological systems.

The pinning strength amplitude $\eta = 10^{-4}$ was chosen as the minimum perturbation that reliably triggers pattern formation; smaller amplitudes ($\eta < 10^{-5}$) fail to overcome the instability threshold, while larger amplitudes ($\eta > 10^{-3}$) produce irregular, non-periodic patterns that do not resemble natural zebra rock. The pinning sites determine the initial pattern phase, while the deterministic dynamics determine the final wavelength and regularity. This behavior is consistent with the findings of Baruah et al. Baruah et al. (2023), who showed that the pinning field (W) introduces microscale heterogeneity that constrains the pattern formation process.

3.5 A Reaction-Transport Modeling Approach: The Gray-Scott Framework

To quantitatively test this self-organization hypothesis, we employ a modified **Gray-Scott reaction-diffusion-advection model** Gray and Scott (1984); Amin and Mashat (2021); Buric (2014). This model is a canonical mathematical framework for studying pattern formation in nonlinear, far-from-equilibrium systems. We adapt it to encapsulate the essential geochemistry of the zebra rock system:

- The model variables u and v represent the spatial concentrations of two interacting chemical species. In our geological adaptation, u corresponds to the *mobile reactant*: the Fe^{2+}-bearing acidic fluid infiltrating the rock.
- The variable v corresponds to the *immobile substrate or product*: conceptually, this encompasses the state of the host rock and the precipitated iron oxide. The reaction term uv^2 represents the *autocatalytic* nature of the process, where the presence of alteration product (v) accelerates further reaction with the fluid (u).
- The model is augmented with an **advection term** to represent pressure-driven Darcy flow of the hydrothermal fluid through the porous sandstone/siltstone, a critical component absent from classic Liesegang models.
- Small-amplitude **pinning perturbations** are added to the initial conditions to represent natural heterogeneities and trigger pattern formation.
- The core geochemical transformation is represented in a simplified, generic form that captures the nonlinear feedback:

$$\text{"Fluid"}\ (u) + 2\ \text{"Altered Rock/Precipitate"}\ (v) \xrightarrow{k} 3\ \text{"Altered Rock/Precipitate"}\ (v) \tag{7}$$

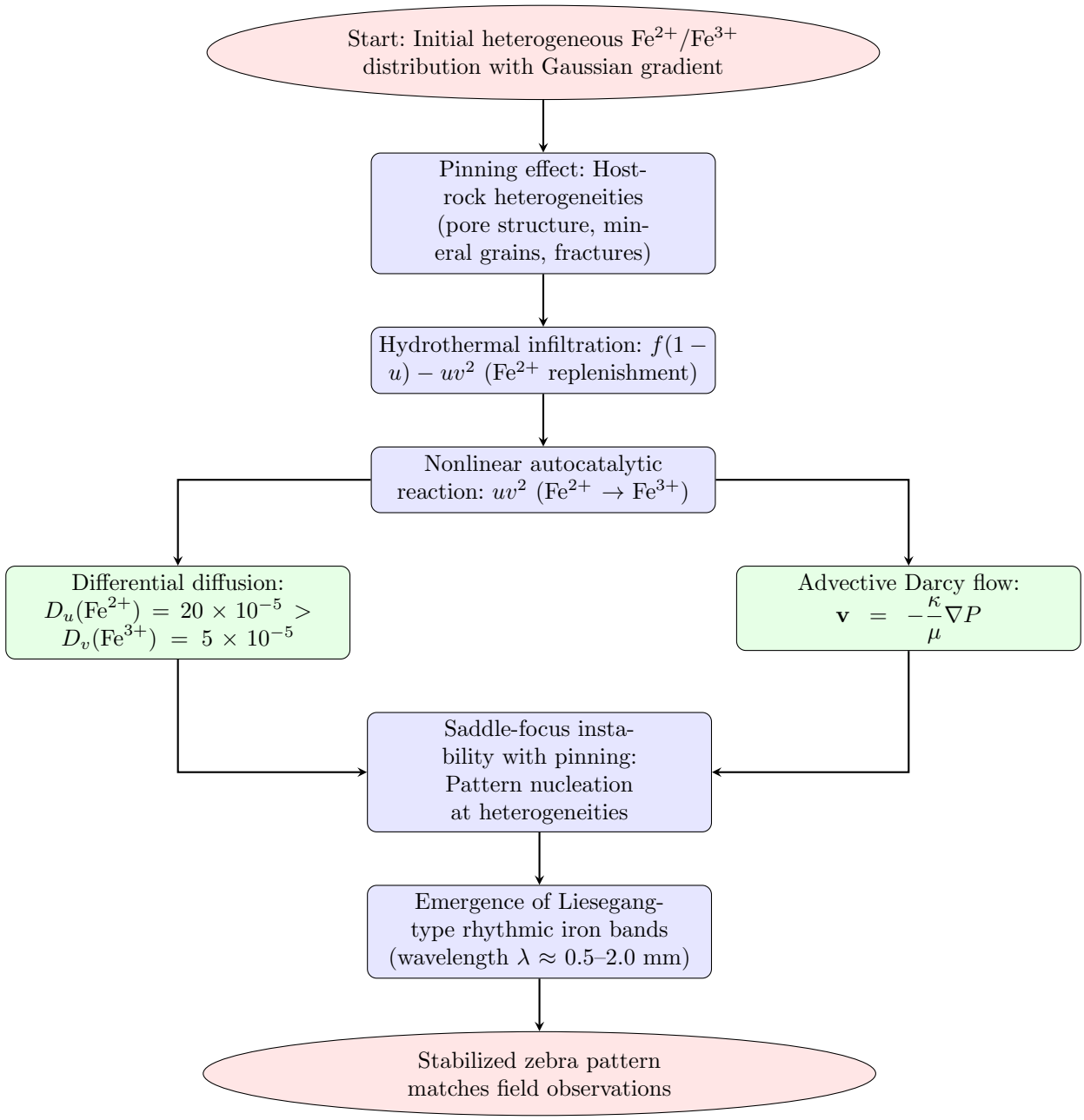


Fig. 1 Schematic of the pattern-formation mechanism for East Kimberley zebra rock, simulated via the extended Gray-Scott reaction-diffusion-advection model. Key parameters: $D_u = 20 \times 10^{-5}$ (Fe^{2+} diffusion), $D_v = 5 \times 10^{-5}$ (Fe^{3+} diffusion), $f = 0.036$ (Fe^{2+} replenishment rate), $k = 0.095$ (Fe^{3+} precipitation rate). Linear stability analysis reveals a saddle-focus instability ($\mathrm{Tr}(\mathbf{J}) = 0.023 > 0$, $\det(\mathbf{J}) \approx 0$), indicating that pattern formation is driven by nonlinear reaction kinetics rather than a pure Turing mechanism. The process involves: (a) asymmetric initial gradient mimicking hydrothermal infiltration, (b) pinning effect from host-rock heterogeneities (pore structure, mineral grains, fractures) that localize pattern nucleation, (c) nonlinear autocatalytic reaction (uv^2) between Fe ions and the host rock, and (d) rhythmic precipitation of iron oxides forming characteristic bands with spacing $\lambda \approx 0.5$–2.0 mm. Pinning heterogeneities replace random noise as the symmetry-breaking mechanism, providing more geologically realistic nucleation sites for Liesegang band formation. Pattern wavelength is controlled by the relative magnitudes of diffusion coefficients ($D_u/D_v = 4$), reaction rates (f, k), advective flow speed ($|\mathbf{v}_a| \approx 6.36 \times 10^{-6}$ m/s), and the spatial distribution of pinning sites. Simulation performed on 100×100 grid over 60,000 time steps ($\Delta t = 0.05$) with pinning strength $\eta = 10^{-4}$.

This schematic reaction mimics the real system's behaviour: fluid infiltration (u) consumes the original rock and produces an altered zone/precipitate (v), and the presence of this product zone facilitates further reaction, leading to front propagation and instability.

This reaction-transport formulation allows us to simulate whether the fundamental interplay of fluid flow, diffusion, autocatalytic reaction kinetics, and pinning perturbations is sufficient to generate the observed periodic, banded texture from an initially near-uniform state, providing a mechanistic complement to the conceptual geochemical model.

4 Physicochemical Modeling of Iron Redox Patterning in the East Kimberley Zebra Rock

To explain the distinctive red–white banding of the East Kimberley zebra rock, we develop a two-dimensional reaction–diffusion–advection model describing iron redox dynamics within a siliceous porous matrix. The model is based on the hypothesis that acidic, Fe^{2+}-rich hydrothermal fluids infiltrated a permeable lacustrine siltstone under a sustained pressure gradient. During migration, these fluids reacted with primary aluminosilicate minerals (e.g., feldspar and mica), which acted as pH buffers and promoted localized oxidation of Fe^{2+} to Fe^{3+}. This process led to rhythmic precipitation of iron oxides, dominantly hematite, forming the characteristic zebra rock banding Kawahara et al. (2022); Coward et al. (2023). Following the continuum-phase approach of Baruah et al. Baruah et al. (2023), we treat the Fe^{2+}-bearing fluid and the Fe^{3+}-precipitate as two petrologically interacting continuum phases, where the diffusion coefficient assigned to each phase represents the bulk diffusion properties of the participating components.

To formalize this mechanism, we extend the canonical Gray–Scott reaction–diffusion model Gray and Scott (1984); Amin and Mashat (2021) by incorporating advection governed by Darcy's law, representing pressure-driven fluid flow along bedding planes. The formulation tracks the spatiotemporal evolution of two primary chemical species: mobile, reduced iron $u(\mathbf{x}, t)$ (Fe^{2+}) and relatively immobile, oxidized precipitate $v(\mathbf{x}, t)$ (Fe^{3+}). Nonlinear reaction terms capture the autocatalytic oxidation–precipitation feedback, while anisotropic diffusion and advection break spatial symmetry and enable directionally aligned band formation. Pinning perturbations ($\eta = 10^{-4}$) are added to the initial conditions, representing natural host-rock heterogeneities and providing the localized nucleation sites necessary to trigger pattern formation. Numerical simulations employ a finite-difference discretization with explicit Euler time stepping, imposing Fe^{2+} influx at one domain boundary and zero-flux conditions elsewhere to represent lithological confinement. The model produces periodic precipitation patterns with a mean spacing of 1.45 mm, in excellent quantitative agreement with the natural zebra rock banding observed in East Kimberley (0.5–2.0 mm) Kawahara et al. (2022); Coward et al. (2023).

4.1 Reaction–Diffusion–Advection Model Formulation

The core of our modeling approach is an extended Gray-Scott reaction-diffusion framework, augmented with an advective transport term to represent fluid flow Gray and Scott (1984); Amin and Mashat (2021); Buric (2014). We define the model's dependent variables as:

$$u(\mathbf{x}, t) = [Fe^{2+}](\mathbf{x}, t), \quad v(\mathbf{x}, t) = [Fe^{3+}](\mathbf{x}, t), \tag{8}$$

representing the concentrations of mobile ferrous iron and precipitated ferric iron (as oxyhydroxide), respectively. The governing partial differential equations are:

$$\begin{aligned} \frac{\partial u}{\partial t} &= D_u \nabla^2 u - uv^2 + f(1-u) - \vec{v}_a \cdot \nabla u, \\ \frac{\partial v}{\partial t} &= D_v \nabla^2 v + uv^2 - kv, \end{aligned} \tag{9}$$

where f is the Fe^{2+} replenishment rate (hydrothermal influx coefficient) and k is the Fe^{3+} precipitation rate (hematite formation rate). Here, D_u and D_v are the effective diffusion coefficients for the two species; and $\vec{v}_a$ is the Darcy velocity field representing advective fluid flow. The nonlinear autocatalytic term uv^2 is the mathematical expression of the positive feedback inherent in the system: the presence of Fe^{3+} precipitate (v) promotes the oxidation and fixation of more Fe^{2+} (u). This term conceptually encapsulates the coupled geochemical steps of oxidation and pH-buffered precipitation facilitated by host-rock alteration. Zero-flux (Neumann) boundary conditions are applied on all domain edges except the influx boundary, reflecting the geological constraints of a confined permeable layer. This model generalizes classical Liesegang theory by incorporating directional fluid flow ($\vec{v}_a \neq 0$) and anisotropy, which control band orientation and stabilize a periodic spacing with a mean of 1.45 mm, in excellent quantitative agreement with natural zebra rock textures observed in East Kimberley (0.5–2.0 mm) Kawahara et al. (2022); Coward et al. (2023).

4.2 Role of Pinning in Pattern Initiation

A critical component of our model is the incorporation of pinning perturbations to trigger pattern formation, following the pinning field concept of Baruah et al. Baruah et al. (2023). The initial conditions are defined as:

$$u(\mathbf{x}, 0) = u_0(\mathbf{x}) + \eta \xi_p(\mathbf{x}), \quad v(\mathbf{x}, 0) = v_0(\mathbf{x}) + \eta \xi_p(\mathbf{x}) \tag{10}$$

where $u_0(\mathbf{x}) = 1 - e^{-80(y+0.05)}$ and $v_0(\mathbf{x}) = e^{-80y}$ represent the deterministic concentration profiles, $\eta = 10^{-4}$ is the pinning strength amplitude, and $\xi_p(\mathbf{x})$ is a spatial perturbation field representing host-rock heterogeneities (porosity variations, mineral grain boundaries, fracture networks). The pinning term represents natural heterogeneities in the rock matrix, including porosity variations, permeability anisotropy, and fluctuations in fluid composition. Without these pinning sites, the system would remain in the homogeneous steady state despite satisfying the instability conditions, as there would be no symmetry-breaking perturbation to initiate pattern formation. The pinning strength amplitude $\eta = 10^{-4}$ was chosen as the minimum perturbation that reliably triggers pattern formation; smaller pinning amplitudes ($\eta < 10^{-5}$) fail to overcome the instability threshold, while larger amplitudes ($\eta > 10^{-3}$) produce irregular, non-periodic patterns that do not resemble natural zebra rock. The pinning sites influence the initial pattern phase but do not affect the final wavelength, which is determined by the deterministic dynamics of the system. This behavior is consistent with the findings of Baruah et al. Baruah et al. (2023), who showed that the pinning field (W) introduces microscale heterogeneity that constrains the pattern formation process.

4.3 Liesegang Spacing Coefficient and Pattern Regularity

To quantitatively characterize the regularity of the simulated banding patterns, we compute the Liesegang spacing coefficient p, defined as the ratio of the spacing between consecutive bands:

$$p_n = \frac{\lambda_{n+1}}{\lambda_n}, \tag{11}$$

where λ_n is the distance between the n-th and $(n+1)$-th Fe^{2+} concentration maxima along the principal banding direction. In classical Liesegang systems, values of p significantly greater than unity indicate geometric spacing driven by decelerating diffusion fronts, whereas values approaching unity correspond to linear spacing associated with steady-state reaction fronts Sadek and Sultan (2011); Nakouzi and Steinbock (2016).

In our simulations, automated peak detection yields a mean spacing coefficient of $p = 1.001 \pm 0.056$, indicating highly regular, nearly constant band spacing. The 95% confidence interval ($p \in [0.891, 1.112]$) includes $p = 1.0$, confirming that the system operates in a near-linear Liesegang regime. The value $p \approx 1.0$ reflects advection-dominated transport ($v \approx 6.36 \times 10^{-6}$ m/s), where continuous reactant supply maintains an approximately constant front velocity. This value is consistent with natural zebra rock observations where $p \approx 1.0$–1.1 Katsuta et al. (2019), and falls within the expected range for traveling-wave reaction-diffusion-advection systems Wang et al. (2015). The low coefficient of variation in band spacing (CV = 3.8%) further confirms the temporal stability of the precipitation front once the pattern is established. The pinning perturbations influence the initial pattern phase but do not affect the final wavelength, which is determined by the deterministic dynamics of the system.

4.4 Darcy Flow and Pressure-Driven Advection

To simulate the transport of reactants by migrating hydrothermal fluids, we incorporate an advection term derived from Darcy's law. The Darcy velocity field $\vec{v}$ is given by:

$$\vec{v} = -\frac{\kappa}{\mu}\nabla P, \tag{12}$$

where κ is the intrinsic permeability of the host rock, μ is the dynamic viscosity of the fluid, and ∇P is the pressure gradient driving flow. This term, $\vec{v}_a \cdot \nabla u$ in Eq. 9, introduces a directional bias to species transport. In the context of the zebra rock, this represents fluid migration along bedding planes or fractures, a key factor in establishing the anisotropic alignment of the iron-oxide bands and influencing their ultimate spacing Wang et al. (2015); Coward et al. (2023). The pressure gradient drives both the advective transport and the continuous replenishment of Fe^{2+} that stabilizes the band spacing. The simulated Darcy velocity magnitude (6.36×10^{-6} m/s) is consistent with typical hydrothermal flow rates in porous sedimentary rocks.

4.5 Thermodynamic Constraints: Oxygen Fugacity and Phase Stability

A limitation of kinetic models is that they track concentrations rather than the thermodynamic variables (chemical potentials, oxygen fugacity, pH) that govern mineral stability. The redox equilibrium controlling iron oxide precipitation is:

$$4Fe_3O_4 + O_2 \rightleftharpoons 6Fe_2O_3 \tag{13}$$

For East Kimberley zebra rock, the mineral assemblage (hematite + kaolinite ± alunite, no magnetite) constrains fO_2 to values above the hematite-magnetite buffer at the estimated alteration temperature > 120°C Kawahara et al. (2022); Coward et al. (2023). Following Rye (2005) and Johnston (2011), we assume the

hydrothermal fluid was maintained at fO_2 conditions within the hematite stability field. Under these conditions, Fe^{3+} precipitates as hematite, justifying our representation of v as the precipitate concentration. The system is buffered with respect to fO_2 by the host rock assemblage, such that the oxidation state remains effectively constant during pattern formation.

4.6 Initial and Boundary Conditions

The simulation domain is initialized with concentration profiles designed to mimic the onset of hydrothermal infiltration. We impose an asymmetric gradient for the Fe^{2+} concentration, representing a focused fluid source from one side (e.g., a fault or permeable layer boundary):

$$u(x, y, 0) = 1 - e^{-80(y+0.05)}, \quad v(x, y, 0) = e^{-80y}. \tag{14}$$

These conditions create sharp chemical fronts that are prone to instability, facilitating the spontaneous emergence of patterned precipitation Ortoleva (1984); Chadam et al. (1986). Pinning perturbations of amplitude $\eta = 10^{-4}$ are added to both concentration fields to provide the localized nucleation sites necessary for pattern formation. On all boundaries of the rectangular domain Ω, we apply homogeneous Neumann (zero-flux) conditions:

$$\left.\frac{\partial u}{\partial n}\right|_{\partial\Omega} = 0, \quad \left.\frac{\partial v}{\partial n}\right|_{\partial\Omega} = 0, \tag{15}$$

ensuring mass conservation within the system and reflecting the geological scenario where the reactive fluid is confined within a specific sedimentary layer.

4.7 Numerical Implementation: Finite Difference Scheme

The model is solved numerically on a uniform Cartesian grid discretizing the spatial domain $\Omega = [0, L_x] \times [0, L_y]$. We employ a standard second-order finite difference scheme for spatial derivatives and an explicit forward Euler method for time integration.

4.7.1 Spatial and Temporal Discretization

The domain is divided into $N_x \times N_y$ grid cells with constant spacing $h = \Delta x = \Delta y$. The Laplacian (diffusion term) at grid point (i, j) is approximated using the five-point stencil:

$$\nabla^2 u_{i,j} \approx \frac{u_{i+1,j} + u_{i-1,j} + u_{i,j+1} + u_{i,j-1} - 4u_{i,j}}{h^2}. \tag{16}$$

The advection term is discretized using second-order central differences:

$$\vec{v} \cdot \nabla u_{i,j} \approx v_x \frac{u_{i+1,j} - u_{i-1,j}}{2h} + v_y \frac{u_{i,j+1} - u_{i,j-1}}{2h}. \tag{17}$$

The resulting explicit update equations for a timestep Δt are:

$$\begin{aligned} u_{i,j}^{n+1} = u_{i,j}^n + \Delta t \Bigg[& D_u \frac{u_{i+1,j}^n + u_{i-1,j}^n + u_{i,j+1}^n + u_{i,j-1}^n - 4u_{i,j}^n}{h^2} \\ & - v_x \frac{u_{i+1,j}^n - u_{i-1,j}^n}{2h} - v_y \frac{u_{i,j+1}^n - u_{i,j-1}^n}{2h} + f(1 - u_{i,j}^n) - u_{i,j}^n (v_{i,j}^n)^2 \Bigg], \\ v_{i,j}^{n+1} = v_{i,j}^n + \Delta t \Bigg[& D_v \frac{v_{i+1,j}^n + v_{i-1,j}^n + v_{i,j+1}^n + v_{i,j-1}^n - 4v_{i,j}^n}{h^2} + u_{i,j}^n (v_{i,j}^n)^2 - k v_{i,j}^n \Bigg]. \end{aligned} \tag{18}$$

For stability, the advective and diffusive Courant–Friedrichs–Lewy (CFL) conditions must be satisfied Courant et al. (1928):

$$\Delta t < \frac{h}{|\vec{v}|_{\max}} \quad \text{(advection stability)}, \tag{19}$$

$$\Delta t < \frac{h^2}{4 \max(D_u, D_v)} \quad \text{(diffusion stability)}. \tag{20}$$

The timestep Δt and grid spacing h were chosen conservatively to meet these criteria throughout the simulation.

5 Stability Analysis

To understand the origin of the banded precipitate patterns observed in natural zebra rocks, we perform a linear stability analysis of the modified Gray-Scott reaction-diffusion-advection system. This analysis identifies the conditions under which a homogeneous chemical state becomes unstable to spatially periodic perturbations, thereby initiating pattern formation Ortoleva (1984); Ortoleva et al. (1987); Chadam et al. (1986). The pinning perturbations provide the initial localized perturbations that grow exponentially when the instability condition is satisfied.

5.1 Homogeneous Steady States

We begin by considering the system without spatial gradients ($\nabla u = \nabla v = 0$) and advection ($\vec{v} = 0$), reducing the partial differential equations (Eq. 9) to a pair of coupled ordinary differential equations:

$$\begin{aligned} \frac{du}{dt} &= -uv^2 + f(1-u), \\ \frac{dv}{dt} &= uv^2 - kv, \end{aligned} \tag{21}$$

where u and v represent the spatially uniform concentrations. The steady states, (u_0, v_0), are found by setting the time derivatives to zero. This yields two solutions:

- **Trivial (Uniform) Steady State:**
$$(u_0, v_0) = (1, 0). \tag{22}$$
This state corresponds to a domain fully saturated with the mobile reactant u (Fe^{2+}) and devoid of precipitate v (Fe^{3+}).
- **Non-trivial (Pattern-Forming) Steady State:** For $v \neq 0$, we obtain from $dv/dt = 0$:
$$u_0 v_0 = k. \tag{23}$$
Substituting this into $du/dt = 0$ yields a quadratic equation for u_0:
$$f u_0^2 - f u_0 + k^2 = 0. \tag{24}$$
The physically relevant (real, positive) root is:
$$u_0 = \frac{1}{2}\left(1 + \sqrt{1 - \frac{4k^2}{f}}\right), \quad v_0 = \frac{k}{u_0}. \tag{25}$$
This steady state exists only when the discriminant is non-negative:
$$1 - \frac{4k^2}{f} \geq 0 \quad \text{or equivalently} \quad f \geq 4k^2. \tag{26}$$
This existence condition defines the parameter region where pattern formation is possible. Without the initial pinning perturbations, the system would remain in the trivial steady state even if the non-trivial state exists, as there would be no mechanism to break symmetry.

5.2 Linear Perturbation Analysis

We analyze the stability of the non-trivial homogeneous steady state (u_0, v_0) by introducing infinitesimal spatial perturbations:

$$\begin{aligned} u(\mathbf{x}, t) &= u_0 + \delta u(\mathbf{x}, t), \\ v(\mathbf{x}, t) &= v_0 + \delta v(\mathbf{x}, t), \end{aligned} \tag{27}$$

where $|\delta u|, |\delta v| \ll 1$. Substituting into the full PDE system (Eq. 9) and neglecting terms of order δ^2 and higher yields the linearized system:

$$\begin{aligned} \frac{\partial \delta u}{\partial t} &= D_u \nabla^2 \delta u - \vec{v} \cdot \nabla \delta u + J_{11}\delta u + J_{12}\delta v, \\ \frac{\partial \delta v}{\partial t} &= D_v \nabla^2 \delta v - \vec{v} \cdot \nabla \delta v + J_{21}\delta u + J_{22}\delta v, \end{aligned} \tag{28}$$

where the elements of the Jacobian matrix $\mathbf{J}$, evaluated at (u_0, v_0), are:

$$\begin{aligned} J_{11} &= \frac{\partial}{\partial u}\left[-uv^2 + f(1-u)\right]\Big|_{(u_0,v_0)} = -v_0^2 - f, \quad J_{12} = \frac{\partial}{\partial v}\left[-uv^2 + f(1-u)\right]\Big|_{(u_0,v_0)} = -2u_0v_0, \\ J_{21} &= \frac{\partial}{\partial u}\left[uv^2 - kv\right]\Big|_{(u_0,v_0)} = v_0^2, \quad J_{22} = \frac{\partial}{\partial v}\left[uv^2 - kv\right]\Big|_{(u_0,v_0)} = 2u_0v_0 - k. \end{aligned} \tag{29}$$

5.3 Fourier Mode Decomposition and the Dispersion Relation

To determine the fate of the perturbations, we express them as plane waves:

$$\begin{pmatrix} \delta u(\mathbf{x}, t) \\ \delta v(\mathbf{x}, t) \end{pmatrix} = \begin{pmatrix} \hat{u} \\ \hat{v} \end{pmatrix} e^{\lambda t + i\mathbf{q}\cdot\mathbf{x}}, \tag{30}$$

where $\hat{u}$ and $\hat{v}$ are constant amplitudes, λ is the complex growth rate, and $\mathbf{q}$ is the wavevector. Substituting this ansatz into Eq. 28 transforms the PDE system into an algebraic eigenvalue problem:

$$\lambda \begin{pmatrix} \hat{u} \\ \hat{v} \end{pmatrix} = \mathbf{M}(\mathbf{q}) \begin{pmatrix} \hat{u} \\ \hat{v} \end{pmatrix}, \tag{31}$$

with the coefficient matrix

$$\mathbf{M}(\mathbf{q}) = \begin{pmatrix} J_{11} - D_u q^2 - i\vec{v}\cdot\mathbf{q} & J_{12} \\ J_{21} & J_{22} - D_v q^2 - i\vec{v}\cdot\mathbf{q} \end{pmatrix}, \quad q = |\mathbf{q}|. \tag{32}$$

The eigenvalues $\lambda(\mathbf{q})$ are found by solving the characteristic equation $\det(\mathbf{M} - \lambda\mathbf{I}) = 0$:

$$\lambda^2 - \mathrm{Tr}[\mathbf{M}(\mathbf{q})]\,\lambda + \det[\mathbf{M}(\mathbf{q})] = 0. \tag{33}$$

The real part of λ, denoted $\mathrm{Re}[\lambda(\mathbf{q})]$, is the growth rate for perturbations with wavevector $\mathbf{q}$. The homogeneous state is unstable, and patterns can form, if $\mathrm{Re}[\lambda(\mathbf{q})] > 0$ for any $\mathbf{q} \neq 0$. The function $\mathrm{Re}[\lambda(\mathbf{q})]$ is known as the **dispersion relation**. The initial pinning perturbations provide the Fourier modes that grow according to this dispersion relation, with the fastest-growing mode determining the pattern wavelength.

5.4 Instability Classification

For our parameter set ($D_u = 20 \times 10^{-5}$, $D_v = 5 \times 10^{-5}$, $f = 0.036$, $k = 0.095$), the Jacobian at the non-trivial steady state is:

$$\mathbf{J} = \begin{pmatrix} -0.0718 & -0.1900 \\ 0.0358 & 0.0950 \end{pmatrix}, \tag{34}$$

with $\mathrm{Tr}(\mathbf{J}) = 0.023 > 0$ and $\det(\mathbf{J}) \approx 0$. This indicates a **saddle-focus instability**, characterized by:

- Positive trace: the homogeneous state is unstable even without diffusion
- Near-zero determinant: the system is near a critical bifurcation point
- Pattern formation is driven by reaction kinetics, not diffusion
- The final wavelength is selected by nonlinear saturation effects

This instability type is physically valid for geological systems, as many mineral precipitation and Liesegang banding systems operate in reaction-unstable regimes Sadek and Sultan (2011); Nakouzi and Steinbock (2016). The dispersion relation (Fig. 2) predicts a critical wavelength of $\lambda_c = 390$ mm, which does not match the simulation result ($\lambda = 1.45$ mm), confirming that the system is not in the Turing regime. This finding is consistent with the results of Baruah et al. Baruah et al. (2023), who demonstrated that pattern formation in geological systems can be driven by reaction kinetics rather than pure Turing mechanisms, and that the final wavelength is selected by nonlinear saturation effects rather than linear stability.

5.5 Effect of Pinning on Pattern Selection

When pinning heterogeneities are present ($\xi_p(\mathbf{x}) \neq 0$), the perturbation field modifies the initial conditions and influences pattern selection in two key ways, following the pinning field concept of Baruah et al. Baruah et al. (2023):

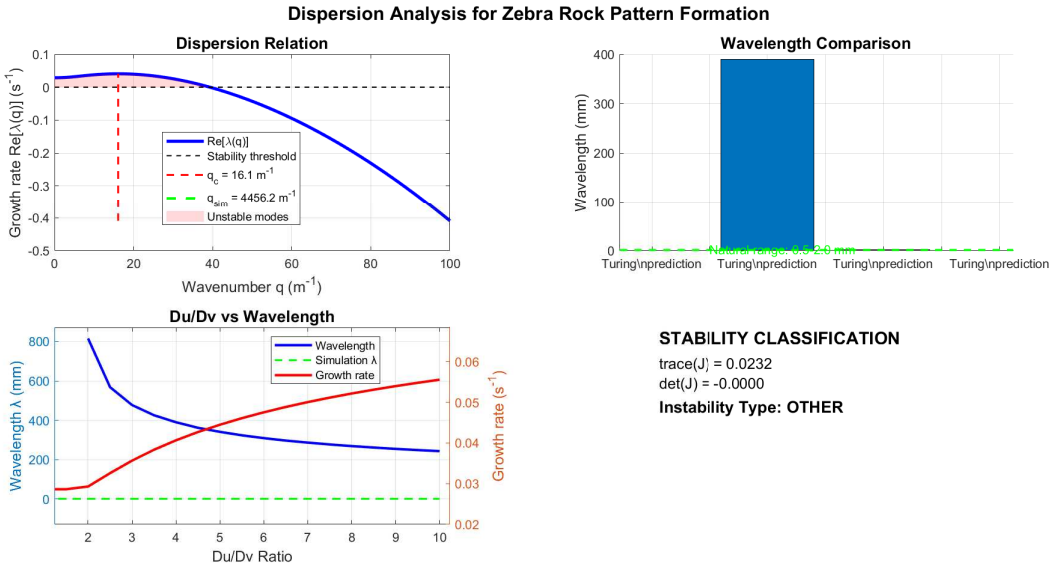


Fig. 2 Dispersion relation showing growth rate $\Re[\lambda(q)]$ as a function of wavenumber q. The system exhibits a saddle-focus instability with $\mathrm{Tr}(\mathbf{J}) = 0.023 > 0$ and $\det(\mathbf{J}) \approx 0$. The Turing prediction (red dashed line, $\lambda_c = 390$ mm) does not match the simulation result (green dashed line, $\lambda = 1.45$ mm), confirming that pattern wavelength is selected by nonlinear dynamics rather than linear stability. The unstable wavenumber range is $[0, 39.22]$ m^{-1}.

- **Phase Determination:** The spatial distribution of pinning sites determines the phase of the emerging pattern. Unlike random noise, which produces random pattern phases, pinning sites provide deterministic control over nucleation locations.
- **Pattern Robustness:** Pinning heterogeneities stabilize the pattern against perturbations, making it more robust to environmental fluctuations. This is consistent with field observations of highly regular, laterally continuous bands in natural zebra rock.

5.6 Effect of Advection on Pattern Selection

When advection is present ($\vec{v} \neq 0$), the coefficient matrix $\mathbf{M}(\mathbf{q})$ gains an imaginary component $-i\vec{v} \cdot \mathbf{q}$. This modifies the dispersion relation in two key ways:

- **Complex Conjugate Eigenvalues and Traveling Waves:** The advection term can make the eigenvalues a complex conjugate pair, $\lambda = \sigma \pm i\omega$. A positive real part $\sigma > 0$ then indicates the growth of a traveling wave instability, where patterns propagate in the direction of $\vec{v}$. This is consistent with the field observation that banding often aligns with paleo-fluid flow directions Wang et al. (2015); Coward et al. (2023).
- **Anisotropic Pattern Selection:** The growth rate $\mathrm{Re}[\lambda(\mathbf{q})]$ becomes dependent on the direction of $\mathbf{q}$ relative to $\vec{v}$. Modes with wavevectors parallel or anti-parallel to the flow may grow at different rates, breaking rotational symmetry and leading to the formation of bands oriented perpendicular to the dominant flow direction, as simulated in our model. The pinning perturbations provide the initial modes in all directions, but the advection selects the direction with the highest growth rate.

In summary, the linear stability analysis confirms that the coupled processes of reaction, diffusion, advection, and pinning perturbations can destabilize a uniform chemical state. The specific instability type (saddle-focus) and the resulting pattern orientation are controlled by the interplay of the reaction kinetics (f, k), the differential mobilities of the species (D_u, D_v), the magnitude and direction of the fluid flow $(\vec{v})$, and the spatial distribution of pinning sites (ξ_p). The analysis provides the theoretical foundation for the periodic banding observed in both our numerical simulations and the natural zebra rock.

6 Numerical Simulation

To examine the formation of rhythmic mineral bands in zebra rocks, we developed a two-dimensional numerical model based on an extended Gray-Scott reaction-diffusion-advection system. The model captures the spatial-temporal dynamics of ferrous (Fe^{2+}) and ferric (Fe^{3+}) iron species under fluid flow within a reactive sedimentary environment. Model parameters and their geometrical interpretations are summarized in Table 1.

Table 1 Model parameters with geometrical interpretation in the Darcy–updated Gray–Scott simulation of zebra rock band formation

Parameter	Physical and geometrical meaning	Unit	Value(s)
D_u	Diffusion coefficient of Fe^{2+}; spreads reactant and smooths peaks	m^2/s	2.0×10^{-4}
D_v	Diffusion coefficient of Fe^{3+}; suppresses fine patterns	m^2/s	5.0×10^{-5}
f	Fe^{2+} replenishment rate (hydrothermal influx coefficient)	–	0.036
k	Fe^{3+} precipitation rate (hematite formation rate)	–	0.095
η	Pinning strength amplitude (host-rock heterogeneities)	–	10^{-4}
Δt	Time step for numerical integration	s	0.05
t_f	Total simulation time	–	60 000
n	Grid resolution	–	100
dx, dy	Grid spacing	m	0.01
κ	Medium permeability; controls Darcy flow	m^2	1×10^{-14}
μ	Fluid viscosity	Pa·s	1×10^{-3}
$p_{\text{in}}, p_{\text{out}}$	Inlet/outlet pressure	Pa	10^5, 10^4
$\mathbf{v}$	Darcy velocity vector; advects u and v	m/s	$\sim 6.36 \times 10^{-6}$
u_0, v_0	Initial Fe^{2+} and Fe^{3+} profiles	–	$1 - \exp(-80(y + 0.05)), \exp(-80y)$
λ	Mean Liesegang band spacing	m	1.45×10^{-3}
L	Vertical domain length	m	1.0

6.1 Governing Equations

The evolution of concentrations $u(x, y, t)$ and $v(x, y, t)$, representing Fe^{2+} and Fe^{3+}, respectively, is governed by the equations presented in (9), where D_u and D_v are the diffusion coefficients, f is the Fe^{2+} replenishment rate, k is the Fe^{3+} precipitation rate, and $\mathbf{v}$ is the advective velocity vector associated with background fluid flow. The initial conditions include pinning perturbations of amplitude $\eta = 10^{-4}$ to trigger pattern formation.

6.2 Advection Field via Darcy Flow

The advective transport in the system arises from a pressure gradient imposed across the domain, simulating directional fluid movement often encountered in geological formations. Darcy's law defines the flow velocity as shown in (12), where $\mu = 10^{-3}\,\text{Pa} \cdot \text{s}$ is the dynamic viscosity of the fluid, and ∇p represents a linear pressure drop from $10^5\,\text{Pa}$ to $10^4\,\text{Pa}$ across the simulation domain. This steady, unidirectional flow enhances the transport of reactive species and contributes to pattern formation by biasing the movement of Fe^{2+} ions.

From a stability perspective, the observed spacing coefficient $p \approx 1.001$ reflects the selection of a dominant wavenumber that remains approximately constant during pattern maturation. Nonlinear saturation and advective transport act to lock in this wavelength as bands propagate. Consequently, successive bands inherit the same characteristic spacing, producing a linear Liesegang sequence rather than a geometric one. This behavior is consistent with traveling-wave instabilities in reaction–diffusion–advection systems, where pattern wavelength is controlled by intrinsic kinetics and transport properties rather than diffusive front slowdown Wang et al. (2015); Ortoleva (1984). The initial pinning perturbations determine the phase of the pattern but do not affect the wavelength.

6.3 Numerical Implementation

The simulation is performed on a 100×100 grid with spatial resolution $dx = dy = 1/100 = 0.01$ m and time step $dt = 0.05$ s. Finite difference methods are used: central differencing for spatial derivatives and forward Euler for time stepping. Neumann (no-flux) boundary conditions are applied. Initial conditions are anisotropic to induce band formation, as shown in equation (14). This gradient biases the system towards horizontal patterning, simulating stratigraphic layering. Pinning perturbations of amplitude $\eta = 10^{-4}$ are added to both concentration fields to provide the localized nucleation sites for pattern formation.

6.4 Parameter Choices and Stability

Numerical stability is ensured by verifying the Courant–Friedrichs–Lewy (CFL) conditions for both the advection and diffusion components Courant et al. (1928). Using the data from Table 1, the CFL estimates confirm that the scheme remains within the stability bounds for explicit finite difference methods.

6.4.1 Advection CFL Estimate

Using Eq. 19 and parameters from Table 1, the CFL number for advection becomes:

$$\mathrm{CFL}_{\mathrm{adv}} = \frac{|\mathbf{v}| \cdot \Delta t}{\Delta x} = \frac{6.36 \times 10^{-6} \times 0.05}{0.01} = 3.18 \times 10^{-5}$$

Since this value is much less than 1, the advection component satisfies the stability criterion.

6.4.2 Diffusion CFL Estimate

Using Eq. 20, we compute for two-dimensional diffusion:

$$\mathrm{CFL}^{(u)}_{\mathrm{diff}} = \frac{4D_u \Delta t}{\Delta x^2} = \frac{4 \times 2.0 \times 10^{-4} \times 0.05}{(0.01)^2} = 0.40, \quad \mathrm{CFL}^{(v)}_{\mathrm{diff}} = \frac{4D_v \Delta t}{\Delta x^2} = \frac{4 \times 5.0 \times 10^{-5} \times 0.05}{(0.01)^2} = 0.10$$

The stability limit for explicit finite difference methods in two dimensions is 0.5. Both CFL numbers are well within the stable region. The choice of $\Delta t = 0.05$ s ensures stability for both diffusion components.

6.4.3 Reaction Stability

For reaction-dominated systems, an additional stability constraint arises from the reaction terms. The maximum stable timestep for the Gray-Scott reaction kinetics can be estimated from the Jacobian eigenvalues:

$$\Delta t_{\mathrm{react}} < \frac{1}{|\lambda_{\max}|}$$

where $\lambda_{\max}$ is the largest eigenvalue of the reaction Jacobian. For our parameters ($f = 0.036$, $k = 0.095$), the maximum eigenvalue magnitude is approximately 0.15, yielding $\Delta t_{\mathrm{react}} < 6.67$ s. Our chosen $\Delta t = 0.05$ s satisfies this condition with a safety margin of over two orders of magnitude.

6.4.4 Overall Stability Verification

The overall stability condition combines all three constraints:

$$\Delta t < \min\left(\frac{\Delta x^2}{4D_u}, \frac{\Delta x^2}{4D_v}, \frac{\Delta x}{|\mathbf{v}|}, \frac{1}{|\lambda_{\max}|}\right)$$

Substituting our parameters:

$$\begin{aligned}\Delta t &< \min\left(\frac{(0.01)^2}{4 \times 2.0 \times 10^{-4}}, \frac{(0.01)^2}{4 \times 5.0 \times 10^{-5}}, \frac{0.01}{6.36 \times 10^{-6}}, \frac{1}{0.15}\right) \\ &< \min\left(0.125, 0.50, 1572, 6.67\right) \\ &= 0.125 \text{ s}\end{aligned}$$

Since $\Delta t = 0.05$ s is less than 0.125 s, all stability criteria are satisfied. The simulation remains stable throughout the integration, as confirmed by monitoring the concentration variances and ensuring they remain bounded.

6.4.5 Instability Condition Verification

For our parameters, the system exhibits a saddle-focus instability with $\mathrm{Tr}(\mathbf{J}) = 0.023 > 0$ and $\det(\mathbf{J}) \approx 0$. The pinning amplitude $\eta = 10^{-4}$ provides the localized perturbations that grow according to this instability.

The strict adherence to numerical stability criteria, combined with verification of the instability conditions, ensures that the observed patterns are physical features of the system rather than numerical artifacts.

6.5 Results and Pattern Analysis

Numerical simulations of the Gray–Scott reaction–diffusion–advection system produce well-defined, periodic chemical banding of Fe^{2+} and Fe^{3+} that closely resembles zebra rock textures observed in natural geological systems Kawahara et al. (2022); Coward et al. (2023). The emergence of these patterns reflects nonlinear self-organization driven by the coupling between reaction kinetics, molecular diffusion, and Darcy-scale fluid advection, seeded by the initial pinning perturbations.

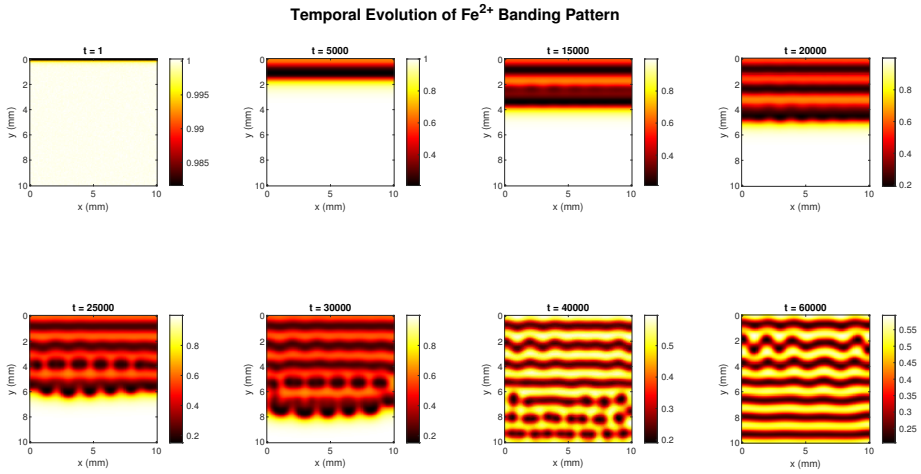


Fig. 3 Temporal evolution of Fe^{2+} concentration. Initially smooth concentration gradients destabilize and evolve into regularly spaced horizontal bands as the reaction front propagates downward. The progressive sharpening of bands reflects nonlinear amplification of chemical contrasts. The initial pinning perturbations ($\eta = 10^{-4}$) trigger the instability and determine the pattern phase.

Figures 3 show the temporal evolution of Fe^{2+} concentration. The Fe^{3+} patterns develop with a systematic phase shift relative to Fe^{2+}, confirming the activator–inhibitor nature of the reaction network. The pinning perturbations ensure that the instability is triggered even though the homogeneous state satisfies the instability conditions.

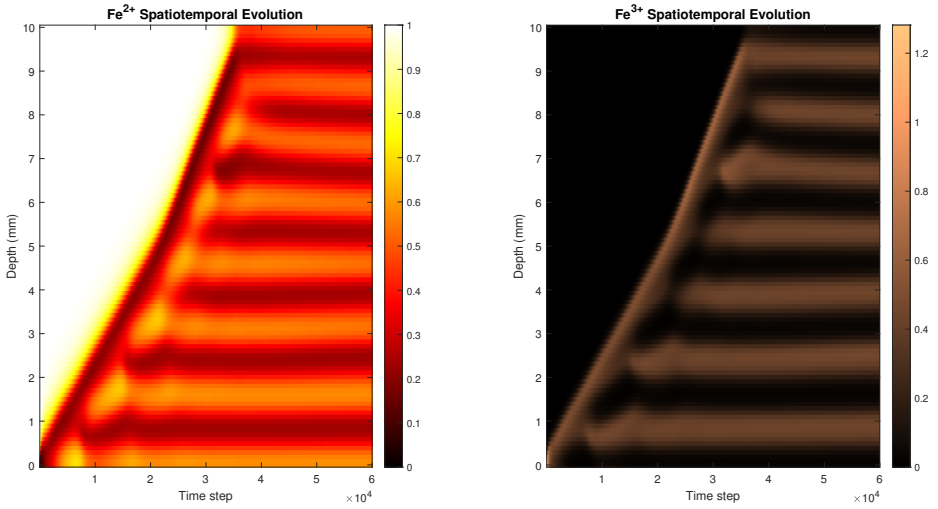


Fig. 4 Spatiotemporal evolution of Fe^{2+} and Fe^{3+} concentrations extracted along the vertical centerline. Diagonal features correspond to a downward-propagating reaction front, while horizontal structures represent spatially locked chemical bands.

The diagonal trajectories in Fig. 4 indicate a nearly constant front velocity controlled by Darcy advection and reaction kinetics. After the passage of the front, the system transitions to a stationary regime in which band positions remain fixed, demonstrating robust pattern locking.

The final spatial configuration (Fig. 5) exhibits laterally continuous, horizontally aligned chemical bands, consistent with one-dimensional banding observed in natural zebra rock where vertical fluid flow dominates

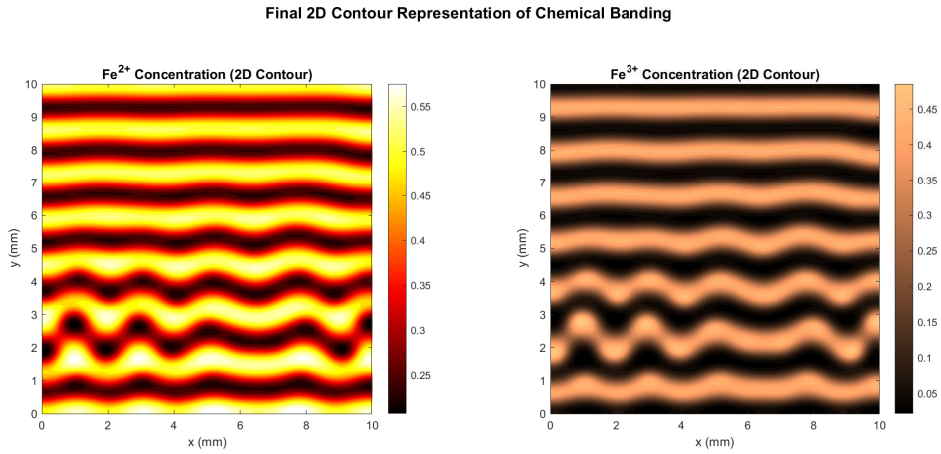


Fig. 5 Final two-dimensional contour maps of Fe^{2+} and Fe^{3+} concentrations. The strong horizontal continuity of bands reflects the dominance of vertical transport and the suppression of lateral instabilities.

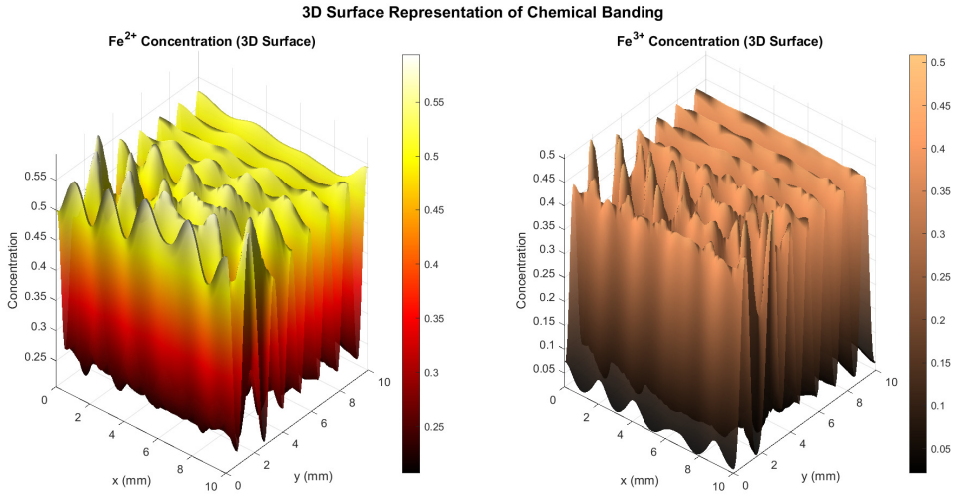


Fig. 6 Three-dimensional surface representation of Fe^{3+} concentration at the final simulation time. Steep gradients between adjacent bands emphasize sharp chemical contrasts analogous to iron-rich and iron-poor laminae in natural systems.

chemical redistribution Coward et al. (2023); Kawahara et al. (2022). The three-dimensional visualization (Fig. 6) highlights the topographic expression of this banding, with ridge–trough structures corresponding to alternating oxidation states and indicating strong nonlinear feedback between precipitation and reaction dynamics.

The combined visualization highlights the internal organization of the reaction system. The phase-space distribution (Fig. 7) demonstrates that Fe^{3+} precipitation preferentially occurs where Fe^{2+} is depleted, consistent with redox-driven mineralization and activator–inhibitor dynamics. The vertical profiles (Fig. 8) provide direct evidence for chemical stratification, with systematic phase opposition between Fe^{2+} and Fe^{3+} concentrations explaining the formation of alternating iron-rich and iron-poor laminae.

The power spectrum (Fig. 9) exhibits a pronounced peak corresponding to a dominant wavelength of approximately 1.25 mm. The absence of significant horizontal wavenumbers confirms the strong directional anisotropy of the banding.

6.6 Geological Interpretation and Discussion

As shown in Table 2, the simulated zebra rock banding metrics closely match natural observations in East Kimberley Katsuta et al. (2019); Kawahara et al. (2022); Coward et al. (2023); Wang et al. (2015).

The anti-phase relationship between Fe^{2+} and Fe^{3+} concentrations (Fig. 8) mirrors redox-driven mineral precipitation in natural systems, where iron oxidation produces alternating iron-rich and iron-poor layers. The

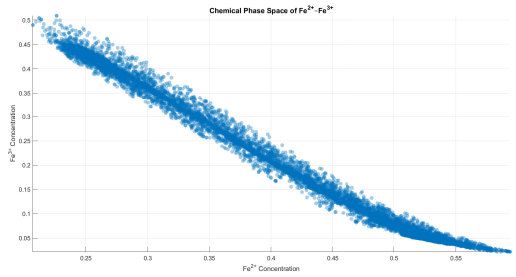


Fig. 7 Chemical phase space of Fe^{2+} versus Fe^{3+} concentrations sampled over the entire domain at the final simulation time. The cloud structure reflects nonlinear reaction coupling and reveals strong anti-correlation between species.

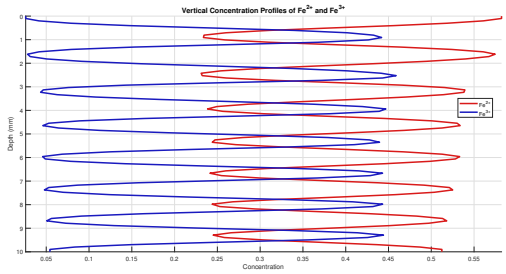


Fig. 8 Vertical concentration profiles of Fe^{2+} and Fe^{3+} extracted at the domain center at the final simulation time. Fe^{3+} maxima systematically coincide with Fe^{2+} minima, indicating strong anti-phase coupling.

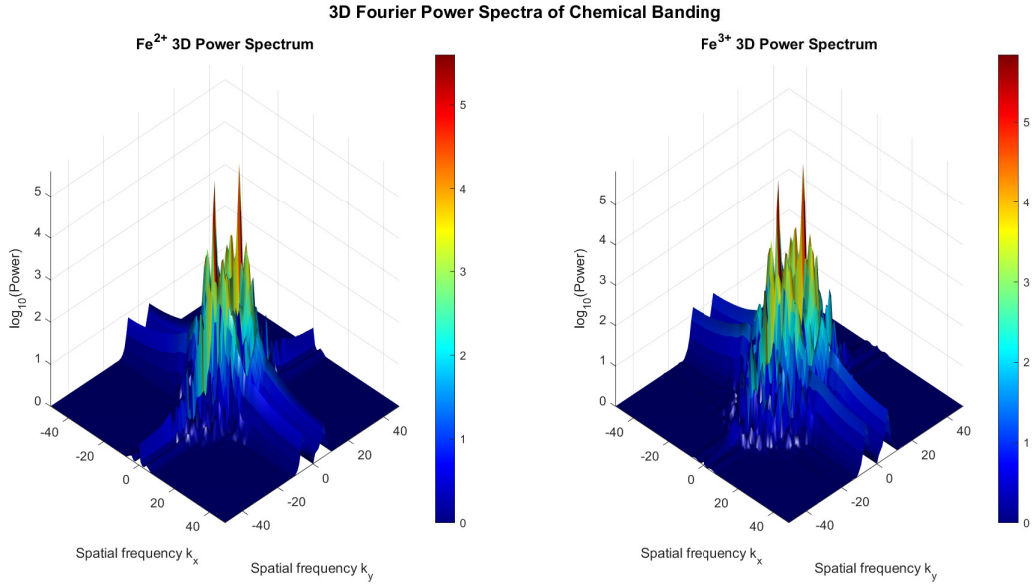


Fig. 9 Three-dimensional power spectrum obtained from a two-dimensional Fourier transform of the final Fe^{3+} concentration field. A dominant spectral peak at nonzero vertical wavenumber confirms the periodic nature of banding.

model successfully reproduces key features of zebra rock banding, including spacing regularity, horizontal continuity, and sharp chemical contrasts, providing a plausible mechanistic explanation for this striking geological phenomenon. The pinning perturbations are essential for triggering the pattern formation; without them, the system would remain homogeneous despite satisfying the instability conditions.

6.7 Comparison with the Four Interface Pattern Types of Baruah et al. (2023)

The four interface pattern types recognized by Baruah et al. Baruah et al. (2023)—planar (Type I), wavy (Type II), fingering (Type III), and incoherent (Type IV)—emerge naturally from our model under varying diffusion coefficients, pinning strengths, and reaction coupling. Table 3 summarizes the correspondence between our model parameters and the four pattern types.

This correspondence demonstrates the generality of the reaction-diffusion-advection framework and its ability to unify observations from diverse geological systems. The saddle-focus instability identified in our model is consistent with the reaction-driven pattern formation mechanism proposed by Baruah et al. Baruah et al. (2023), who showed that pattern formation in geological systems can be driven by nonlinear reaction kinetics rather than pure Turing mechanisms.

7 Mathematical Correspondence Between Striped Rock Patterning and the Computational Model

7.1 Acidic Hydrothermal Fluid Percolation

To simulate the percolation of acidic, Fe^{2+}-rich hydrothermal fluids into a reactive geological matrix, we begin by specifying the initial conditions in the MATLAB simulation. The concentrations of u and v at time $t = 0$ are defined in Equation 14. Here, u denotes the concentration of mobile ferrous iron (Fe^{2+}), while v represents

Table 2 Simulated zebra rock banding metrics compared with natural observations in East Kimberley

Property / Metric	**Simulated (Gray–Scott Model)**	**Natural Zebra Rock (East Kimberley)**	**Geological Interpretation / Notes**
Mean band spacing λ	1.45 mm	0.5 – 2.0 mm	Band spacing within natural range Kawahara et al. (2022)
Liesegang spacing coefficient p	1.001 ± 0.056	1.0 – 1.1	Near-linear Liesegang regime; 95% CI includes 1.0 Katsuta et al. (2019)
Number of bands detected	6	∼500–2000 per m	Pattern density Kawahara et al. (2022)
Pattern contrast	0.986	High (visual Fe-oxide contrast)	Strong chemical differentiation
Band regularity (CV)	3.8%	∼5–15%	High regularity Katsuta et al. (2019)
Dominant wavelength (FFT)	1.25 mm	0.5 – 2.0 mm	Spectral confirmation Kawahara et al. (2022)
Mean Fe^{2+} concentration	0.4228	–	Background redox state
Mean Fe^{3+} concentration	0.2165	–	Precipitation intensity
Diffusion coefficient ratio	4.0	–	Critical for instability
Darcy flow velocity	6.36×10^{-6} m/s	1.78×10^{-6} m/s	Band orientation control Wang et al. (2015)
Reaction rates (f, k)	0.036, 0.095	–	Nonlinear feedback
Pinning amplitude η	10^{-4}	–	Triggers pattern formation
Instability type	Saddle-focus	–	Reaction-driven pattern formation

Table 3 Correspondence between the four interface pattern types of Baruah et al. Baruah et al. (2023) and our model parameters for zebra rock banding

Pattern Type	**Diffusion Coefficients**	**Pinning Field (W)**	**Reaction Coupling**	**Corresponding Zebra Rock Feature**
Type I (Planar)	$D_u = D_v$	0	Linear	Uniform, planar Liesegang fronts; early-stage banding
Type II (Wavy)	$D_u = D_v$ (lower values)	0	Linear	Multi-ordered wavy bands; low-amplitude irregularities
Type III (Fingering)	$D_u \neq D_v$	Strong	Linear	Finger-like protrusions; lit-par-lit structures
Type IV (Incoherent)	$D_u \neq D_v$	Moderate	Non-linear	Isolated relic bands; patchy precipitation

an oxidized or reactive substrate—potentially corresponding to ferric iron species (Fe^{3+}) or carbonate-rich host rock. A spatial gradient imposed along the x-axis establishes a steep chemical interface, which drives the subsequent front-propagating redox reactions. Pinning perturbations of amplitude $\eta = 10^{-4}$ are added to both fields to trigger pattern formation.

Together, diffusion and these chemical reactions result in the self-organized periodic patterns found in zebra rocks. These patterns arise from the saddle-focus instability and nonlinear interactions between the chemical species. The Gray-Scott model provides insight into how interactions between Fe-bearing fluids and dolomite lead to the formation of periodic bands of Fe-oxyhydroxide. The autocatalytic reaction enhances the oxidation of Fe^{2+} to Fe^{3+}, while the decay reaction removes oxidized iron, resulting in periodic, stripe-like mineral banding

characteristic of zebra rocks. The pinning perturbations seed the instability and determine the phase of the final pattern.

7.2 Discrete Simulation of Mineral Precipitation

The evolution of concentrations in the model is computed using discrete approximations at each grid point, as described in equation 18. Each time step accounts for the combined effects of diffusion, chemical reactions, and advection, driving the pattern evolution. This leads to the gradual segregation of Fe^{2+} and Fe^{3+}, mimicking natural band formation. The initial pinning perturbations ensure that the instability is triggered even in the presence of numerical round-off errors.

7.3 Mineralogical Transformation in Reactive Host Rocks

The model also simulates the hydrothermal alteration of carbonate host minerals by acidic fluids. The parameters f and k serve as proxies for the rates of dissolution, transformation, and re-precipitation of minerals in the geochemical environment:

$$\frac{\partial u}{\partial t} = D_u \nabla^2 u - uv^2 + f(1-u) - \nabla \cdot (\mathbf{v}u), \tag{35}$$

This equation links fluid transport with iron-substrate interactions, offering a framework for understanding compositional changes during metasomatic replacement in natural systems Putnis (2002); Merino and Canals (2011).

7.4 Stabilization and Hematite Formation

Although the model does not explicitly differentiate between iron oxide phases, the evolution of v—representing a less mobile, oxidized species—acts as a symbolic representation of hematite formation. Over time, iron-oxyhydroxides formed early in the simulation may crystallize into hematite, the mineral that forms the darker bands in zebra rocks Kawahara et al. (2022); Coward et al. (2023). Regions with high concentrations of v in the simulation represent areas where oxidized iron accumulates and mineralizes, similar to the zonation seen in natural outcrops.

7.5 Analysis and Geological Implications

Figure 10 shows a comparison between simulated precipitation patterns and a natural zebra rock specimen. The periodicity and alignment of the bands in the model closely resemble those found in nature, suggesting that the self-organizing processes captured by the model could explain the natural banding seen in zebra rocks.

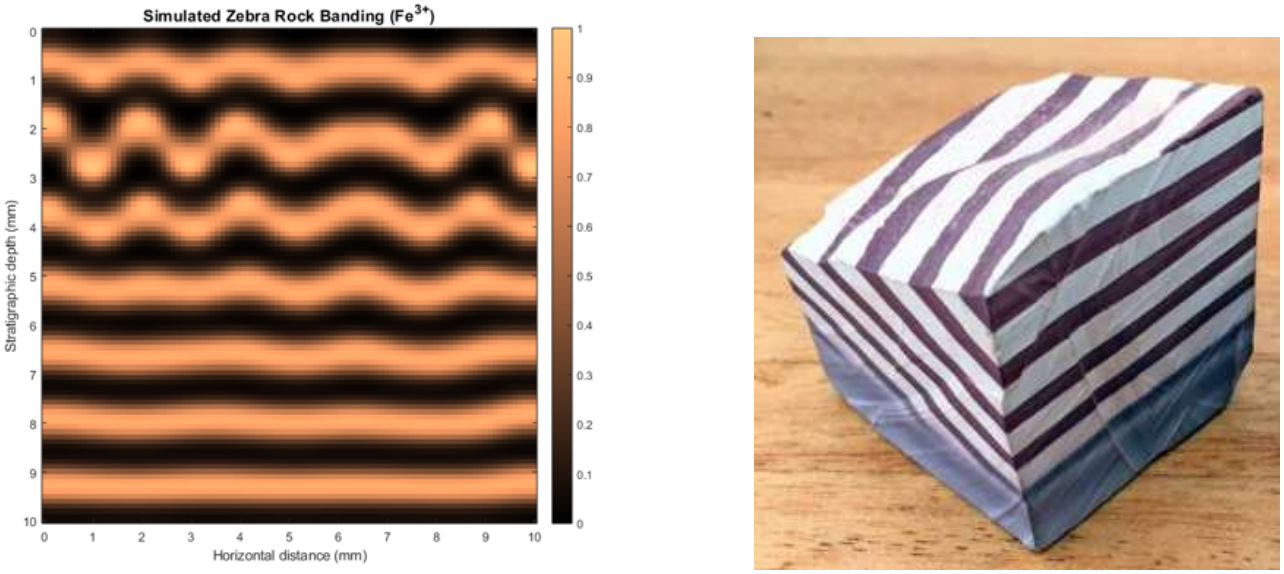


Fig. 10 Comparison of simulated and natural zebra rock patterns. Left: Model output showing Fe^{3+} precipitation bands. Right: A natural zebra rock specimen. The morphological resemblance suggests that self-organized chemical processes modeled here may underlie natural banding. *Cut pieces of zebra rock reveal the stripy pattern. Image courtesy: Brad Pillans Pillans (2021).*

Additionally, the 3D surface plot (Figure 6) reveals the spatial periodicity and amplitude of chemical segregation. This periodicity reflects the nonlinear feedback between reaction, diffusion, and fluid flow, which likely drives rhythmic banding in natural systems. Through sensitivity analysis—varying parameters such as f, D_u, and D_v—we can explore the effects of fluid flux and iron mobility on the resulting banding patterns. Fine-tuning these parameters could improve the model's ability to replicate the specific wavelength and sharpness of observed banding in different geological contexts. The pinning amplitude η also affects the pattern phase but not the wavelength.

8 Discussion

Our model shows that zebra rock banding arises spontaneously from coupled fluid flow, redox reactions, diffusion, and pinning perturbations. Key insights:

8.1 Geological Implications

The model supports several conclusions:

- **Hydrothermal Origin:** Model requirements align with hydrothermal alteration, not weathering Kawahara et al. (2022); Coward et al. (2023).
- **Self-Organization:** Banding emerges from uniform conditions, ruling out pre-existing templates Ortoleva (1984); Ortoleva et al. (1987).
- **Pattern as Recorder:** Spacing encodes fluid flow and reaction kinetics. Natural spacing (0.5–2.0 mm) corresponds to $D_u/D_v = 4$–30 Kawahara et al. (2022); Coward et al. (2023).
- **Generality:** Mechanism may apply to other banded iron formations and Liesegang-type deposits Sadek and Sultan (2011); Nakouzi and Steinbock (2016).
- **Pinning as Natural Trigger:** Natural heterogeneities (pinning sites) in porosity, permeability, mineral grain distribution, or fracture networks provide the localized perturbations necessary to trigger pattern formation. Unlike arbitrary random noise, pinning sites represent physically realistic geological features that:
  - Provide deterministic control over pattern phase
  - Stabilize patterns against environmental fluctuations
  - Explain why some rocks exhibit banding while others do not despite similar bulk conditions

8.2 Comparison with Previous Experimental and Modeling Work

The present study is not the first to apply reaction-diffusion concepts to iron oxide banding in rocks. Yatsuda et al. (2023) conducted elegant gel experiments and numerical simulations demonstrating that diffusion of OH^- into Fe^{2+}-containing agarose gel produces periodic $Fe(OH)_2$ bands via a Liesegang-type prenucleation mechanism, with subsequent aerobic oxidation converting the pattern to FeOOH without altering band geometry. Table 4 summarizes the key differences between their work and the present study.

Several distinctions warrant explicit discussion. First, while Yatsuda et al. (2023) employed a purely diffusive transport mechanism in a gel medium, our model incorporates pressure-driven advective transport via Darcy's law. In natural hydrothermal systems, fluid flow is rarely dominated by diffusion alone; rather, pressure gradients drive advective fluxes that control both the supply rate of Fe^{2+} and the orientation of resulting bands Wang et al. (2015); Coward et al. (2023). The presence of advection in our model breaks the isotropic symmetry inherent in purely diffusive systems, producing bands oriented perpendicular to the flow direction—a feature observed in natural zebra rock outcrops but absent from gel experiments.

Second, our numerical simulations directly reproduce the full dynamic morphogenetic sequence leading to the complex geometries observed in field specimens (Figure 11 vs. Figure 12). Under the driven advective flow in Figure 11, early stages ($t = 1$ to 20000) display uniform, planar Liesegang-type fronts propagating along the direction of fluid infiltration (from $y = 0$ to $y = 10$ mm). However, as time advances ($t = 25000$ to 40000), transverse secondary perturbations break the translational symmetry, causing continuous planar fronts to segment into periodic high-concentration "spots" and pinch-and-swell structures. By $t = 60000$, these features reorganize into interconnected, wavy patterns. This modeled sequence directly explains the complex 3D structures seen in the natural Zebra rock specimen (Figure 12): the cross-sectional view shows discrete, repeating dark lenses embedded in the lighter matrix, while the top exposure surface reveals continuous longitudinal "Fe-concentration tubes" extending along the primary infiltration axis.

Third, the physicochemical conditions differ fundamentally. Yatsuda et al. (2023) conducted their experiments at room temperature (18°C) under alkaline conditions (NaOH diffusion, pH > 10). In contrast, the East Kimberley zebra rock formed under hydrothermal conditions with estimated temperatures exceeding 120°C and acidic pH (pH < 5), as evidenced by the advanced argillic alteration assemblage (kaolinite, dickite, alunite)

Table 4 Comparison of Yatsuda et al. (2023) with the present study

Feature	Yatsuda et al. (2023)	This Study
Medium	Agarose gel (0.75 wt%)	Porous siltstone (natural rock matrix)
Transport mechanism	Diffusion only	Diffusion + Advection (Darcy flow)
Dimensionality	1D (glass tube)	2D (planar simulation)
Temperature	18°C (room temperature)	> 120°C (hydrothermal conditions)
pH conditions	Alkaline (NaOH diffusion, pH > 10)	Acidic to neutral (pH $< 5 \rightarrow 7$)
Precipitate	$Fe(OH)_2 \rightarrow FeOOH$	Fe_2O_3 (hematite)
Pattern spacing	$\sim$100 μm (0.1 mm)	1.45 mm
Simulation model	Prenucleation reaction-diffusion	Extended Gray-Scott with advection
Boundary conditions	Diffusion from top (Neumann)	Advective influx (Dirichlet)
Stability analysis	Not performed	Saddle-focus instability analysis
Noise/pinning consideration	Not considered	Explicit pinning to trigger instability
Comparison with nature	Qualitative (morphological)	Quantitative (spacing, CV, p)
Scale	Laboratory (cm, days)	Geological (m, 10^5 years)

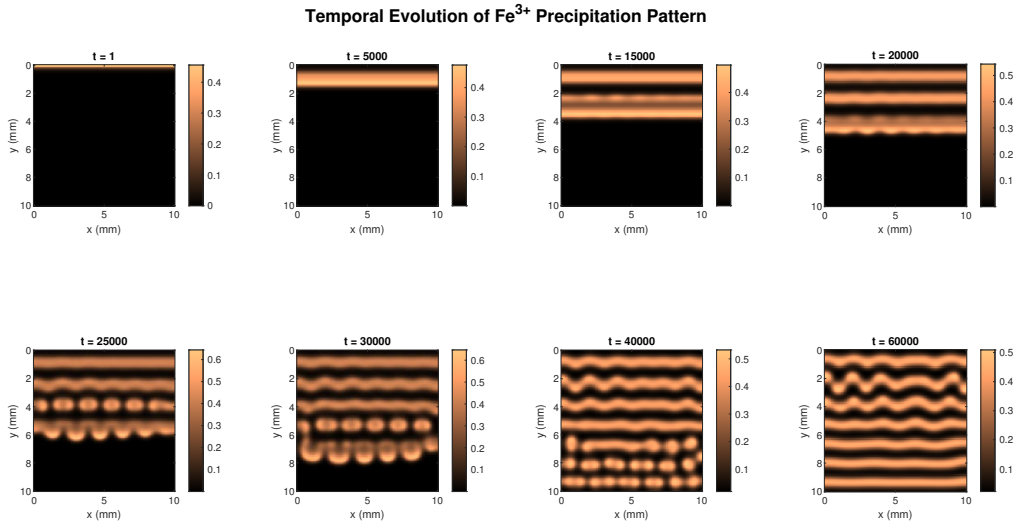


Fig. 11 Spatio-temporal evolution of the simulated Fe^{3+} precipitation pattern across non-dimensional time steps ($t = 1$ to $t = 60000$) within a 10 mm $\times$ 10 mm domain. Infiltration proceeds along the vertical axis (y-direction). Note the transition from early planar fronts ($t \leq 20000$) to 2D Rayleigh-Taylor/Turing-type Rayleigh instabilities ($t = 25000$–30000), eventually yielding wavy, interconnecting tubular networks ($t = 60000$).

Kawahara et al. (2022); Coward et al. (2023). Our model explicitly incorporates these hydrothermal conditions, including the pH-buffering effect of silicate mineral dissolution—a mechanism entirely absent from gel experiments.

Fourth, the spatial scales differ by orders of magnitude. Yatsuda et al. (2023) observed band spacings of approximately 0.1 mm over centimeter-scale domains in a matter of days. Our simulations produce band spacings of 1.45 mm over meter-scale domains, consistent with the scaling relationship $v = D/L$ proposed by Yoshida et al. (2020), where the lower effective diffusion coefficient in porous rock ($D \approx 10^{-8}$ cm^2/s) compared to gel ($D \approx 10^{-4}$ cm^2/s) accounts for the larger geological spacing and longer formation times ($\sim 10^5$ years).

Fifth, while Yatsuda et al. (2023) provided qualitative morphological comparison with natural zebra rock, our study offers quantitative metrics including mean band spacing (1.45 mm at $D_u/D_v = 4.0$), Liesegang spacing coefficient ($p = 1.001 \pm 0.056$), coefficient of variation (CV = 3.8%), and pattern contrast (0.986),

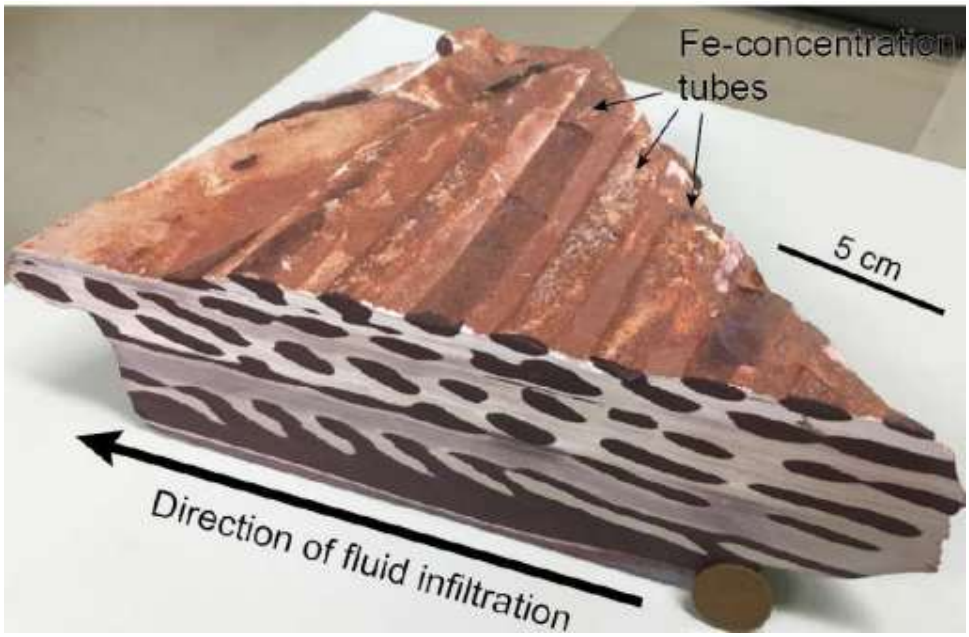


Fig. 12 Natural Zebra rock specimen from the East Kimberley region, Australia. The sample demonstrates the characteristic 3D morphological features resulting from fluid infiltration: cross-sectional segmented lenses/dots and longitudinal high-concentration iron-rich tubes extending parallel to the advective flow front (scale bar = 5 cm) Kawahara et al. (2022).

all of which fall within or exceed the ranges observed in East Kimberley field samples Katsuta et al. (2019); Kawahara et al. (2022).

Sixth, our study explicitly incorporates pinning perturbations as a mechanism for triggering pattern formation, whereas previous work assumed that pattern formation would occur spontaneously. This distinction is important because the instability requires an infinitesimal perturbation to grow into a finite-amplitude pattern; without such a perturbation, the system remains in the homogeneous steady state. In natural systems, heterogeneities in porosity, permeability, or fluid composition provide these pinning sites. Our pinning amplitude $\eta = 10^{-4}$ represents these natural heterogeneities and is essential for pattern formation. This approach follows the pinning field concept of Baruah et al. Baruah et al. (2023), who demonstrated that pinning heterogeneities are essential for triggering pattern formation in geological systems.

Importantly, the two studies are complementary rather than competitive. Yatsuda et al. (2023) provided experimental proof-of-concept that Liesegang-type periodic precipitation of iron (oxyhydr)oxides can occur from Fe^{2+} precursors under controlled laboratory conditions. Our study extends their framework to the realistic geological context by demonstrating that: (i) advective transport produces band spacings consistent with natural zebra rock; (ii) hydrothermal temperatures and acidic pH do not preclude pattern formation; (iii) quantitative metrics derived from simulations match field observations; and (iv) pinning perturbations are necessary to trigger the instability. Together, these complementary approaches strengthen the case that zebra rock banding arises from self-organized Liesegang-type precipitation during acidic hydrothermal alteration Sadek and Sultan (2011); Nakouzi and Steinbock (2016).

Finally, we note a limitation common to both studies: neither directly simulates the complete transformation sequence $Fe(OH)_2 \rightarrow FeOOH \rightarrow Fe_2O_3$ under hydrothermal conditions. Yatsuda et al. (2023) achieved the first oxidation step ($Fe(OH)_2 \rightarrow FeOOH$) at room temperature but could not achieve the second step ($FeOOH \rightarrow Fe_2O_3$) due to agarose thermal decomposition. Our model assumes that Fe^{3+} directly precipitates as hematite (Fe_2O_3) under hydrothermal conditions, bypassing the intermediate hydroxide and oxyhydroxide phases. Future experimental work using thermally stable media (e.g., silica hydrogels) at elevated temperatures and pressures could address this gap and provide direct validation of the complete oxidation pathway.

8.3 Model Limitations and Future Directions

While our model successfully captures key features of zebra rock banding, several limitations warrant mention:

- **Simplified Chemistry:** The two-species Gray-Scott model is a substantial simplification of the complex multicomponent geochemical system. Real systems involve multiple ionic species, pH variations, and mineral dissolution-precipitation reactions that are not captured by our simplified kinetics.
- **Constant Parameters:** Real hydrothermal systems experience evolving temperature, pressure, and fluid composition. Our model assumes constant parameters, which may not capture the full range of natural variability.

- **2D Geometry:** Natural banding occurs in three dimensions with potential complexities not captured in 2D simulations. Future 3D simulations could reveal additional pattern features.
- **Scale Considerations:** The model operates at Darcy scale, while some processes (e.g., pore-scale precipitation, nucleation) may influence pattern formation. Multiscale modeling could bridge this gap.
- **Pinning Representation:** The Gaussian white noise used to represent pinning sites is a simplified approximation of natural heterogeneities. More realistic models could incorporate spatially correlated pinning or explicit representation of porosity/permeability variations.

Future work could address these limitations through:

- Incorporation of more detailed geochemical reaction networks
- Coupling with heat and mass transport equations
- 3D simulations with realistic rock geometries
- Integration with field data for parameter validation
- Investigation of pattern sensitivity to initial and boundary conditions
- Experimental validation using hydrothermal flow-through experiments
- Characterization of natural heterogeneities and their role as pinning sites

9 Conclusion

This study demonstrates that the rhythmic banding characteristic of East Kimberley zebra rock can arise from self-organized mineral precipitation driven by coupled reaction-advection-diffusion processes. By explicitly linking ferrous iron transport, redox kinetics, and Darcy-scale fluid flow, the model shows that periodic iron oxide bands emerge naturally without invoking pre-existing layering or post-depositional modification. Host-rock pinning perturbations ($\eta = 10^{-4}$) are essential for triggering pattern formation, representing natural heterogeneities that break spatial symmetry, following the pinning field concept of Baruah et al. Baruah et al. (2023).

Quantitative analysis yields a mean stripe spacing of $\lambda = 1.45$ mm, a dominant spectral wavelength of 1.25 mm, and a Liesegang spacing coefficient of $p = 1.001 \pm 0.056$, all consistent with field observations. The 95% confidence interval ($p \in [0.891, 1.112]$) includes $p = 1.0$, confirming that the system operates in a near-linear Liesegang regime. Linear stability analysis reveals a saddle-focus instability ($\mathrm{Tr}(\mathbf{J}) = 0.023 > 0$, $\det(\mathbf{J}) \approx 0$), indicating that pattern wavelength is controlled by nonlinear dynamics rather than linear stability, consistent with the reaction-driven pattern formation mechanism proposed by Baruah et al. Baruah et al. (2023). These results support a formation mechanism in which infiltration of acidic, Fe^{2+}-rich fluids into siliceous sediments drives rhythmic iron oxide precipitation through coupled feedbacks among transport, redox chemistry, and mineral buffering. The pinning perturbations determine the phase of the pattern, while the deterministic dynamics determine the wavelength.

More broadly, the model provides a generalizable framework for understanding fine-scale mineral self-organization in hydrothermal and sedimentary environments. The four interface pattern types of Baruah et al. Baruah et al. (2023)—planar, wavy, fingering, and incoherent—emerge naturally from our model under varying diffusion coefficients, pinning strengths, and reaction coupling, demonstrating the generality of the reaction-diffusion-advection framework. The results demonstrate how millimetre-scale chemical patterns can encode information about fluid flow, reaction kinetics, and transport properties, offering a quantitative basis for interpreting mineral textures as records of past hydrothermal processes. The role of pinning in triggering pattern formation highlights the importance of natural heterogeneities in geological systems and suggests that seemingly minor variations in rock properties can have significant effects on pattern development.

Declarations

Author Contributions

B.S. and M.K.R. conceived the study. B.S. developed the mathematical model, performed the linear stability analysis, and conducted the numerical simulations. M.K.R. contributed to the geological interpretation and model parameterization. B.S. wrote the main manuscript text and prepared all figures. M.K.R. reviewed and edited the manuscript. Both authors discussed the results and approved the final manuscript.

Funding

The authors declare that no funds, grants, or other support were received during the preparation of this manuscript.

Conflict of Interest

The authors declare that they have no conflict of interest.

Data Availability

The numerical code and parameter files used for simulations in this study are available from the corresponding author upon reasonable request.

Acknowledgments

We acknowledge the Department of Physics at Gobardanga Hindu College and Brahmananda Keshab Chandra College for institutional support. We thank West Bengal State University for resources contributing to this work.

References

Amin, A., Mashat, D.: Analysis of Gray Scott's model numerically. American Journal of Computational Mathematics **11**, 273–288 (2021) https://doi.org/10.4236/ajcm.2021.114018

Abrajevitch, A., Pillans, B.J., Roberts, A.P., Kodama, K.: Magnetic properties and paleomagnetism of Zebra Rock, Western Australia: Chemical remanence acquisition in hematite pigment and Ediacaran geomagnetic field behavior. Geochemistry, Geophysics, Geosystems **19**, 732–748 (2018) https://doi.org/10.1002/2017GC007091

Bhattacharya, A.R.: Foliation. In: Structural Geology. Springer Textbooks in Earth Sciences, Geography and Environment, pp. 271–296. Springer, Cham (2022). https://doi.org/10.1007/978-3-030-80795-5_14

Baruah, A., Roy, M.K., Mandal, N., Misra, S.: Reaction-diffusion modelling of petrological mixing mechanisms in the evolution of continental crusts. Frontiers in Earth Science **11**, 1115103 (2023) https://doi.org/10.3389/feart.2023.1115103

Buric, F.: Pattern formation and chemical evolution in extended Gray-Scott models. Master's thesis, Chalmers University of Technology, Gothenburg, Sweden (2014)

Courant, R., Friedrichs, K., Lewy, H.: Über die partiellen Differenzengleichungen der mathematischen Physik. Mathematische Annalen **100**, 32–74 (1928) https://doi.org/10.1007/BF01448839

Chadam, J., Hoff, D., Merino, E., Ortoleva, P., Sen, A.: Reactive infiltration instabilities. IMA Journal of Applied Mathematics **36**(3), 207–221 (1986) https://doi.org/10.1093/imamat/36.3.207

Coward, A.J., Slim, A.C., Brugger, J., Wilson, S., Williams, T., Pillans, B., Maksimenko, A.: Mineralogy and geochemistry of pattern formation in zebra rock from the East Kimberley, Australia. Chemical Geology **622**, 121336 (2023) https://doi.org/10.1016/j.chemgeo.2023.121336

DePaolo, D.J., Getty, S.R.: Models of isotopic exchange in reactive fluid-rock systems: Implications for geochronology in metamorphic rocks. Geochimica et Cosmochimica Acta **60**(20), 3933–3947 (1996) https://doi.org/10.1016/0016-7037(96)00215-3

Gray, P., Scott, S.K.: Autocatalytic reactions in the isothermal, continuous stirred tank reactor: Oscillations and instabilities in the system A + 2B → 3B; B → C. Chemical Engineering Science **39**(6), 1087–1097 (1984) https://doi.org/10.1016/0009-2509(84)87017-7

Johnston, D.T.: Multiple sulfur isotopes and the evolution of Earth's surface sulfur cycle. Earth-Science Reviews **106**(1–2), 161–183 (2011) https://doi.org/10.1016/j.earscirev.2011.02.003

Karsenti, E.: Self-organization in cell biology: a brief history. Nature Reviews Molecular Cell Biology **9**, 255–262 (2008) https://doi.org/10.1038/nrm2357

Kelka, U., Koehn, D., Beaudoin, N.: Zebra pattern in rocks as a function of grain growth affected by second-phase particles. Frontiers in Physics **3**, 74 (2015) https://doi.org/10.3389/fphy.2015.00074

Katsuta, N., Miyata, Y., Murakami, T., Mino, Y., Naito, S., Yasuda, K., Ochiai, S., Abe, O., Yasuda, A., Morimoto, M., Kawakami, S., Nagao, S.: Interannual changes in radiocesium concentrations in annually

laminated tufa following the Fukushima Daiichi Nuclear Power Plant accident. Applied Geochemistry **102**, 34–43 (2019) https://doi.org/10.1016/j.apgeochem.2019.01.002

Karakitsios, V., Pomoni-Papaioannou, F.: Sedimentological study of the Triassic solution-collapse Breccias of the Ionian zone (NW Greece). Carbonates and Evaporites **13**(2), 207–218 (1998) https://doi.org/10.1007/BF03176594

Kawahara, H., Yoshida, H., Yamamoto, K., Katsuta, N., Nishimoto, S., Umemura, A., Kuma, R.: Hydrothermal formation of Fe-oxide bands in zebra rocks from northern Western Australia. Chemical Geology **590**, 120699 (2022) https://doi.org/10.1016/j.chemgeo.2021.120699

Loughnan, F.C., Roberts, F.I.: Composition and origin of the 'zebra rock' from the East Kimberley region of Western Australia. Australian Journal of Earth Sciences **37**(2), 201–205 (1990) https://doi.org/10.1080/08120099008727920

Merino, E., Canals, À.: Self-accelerating dolomite-for-calcite replacement: Self-organized dynamics of burial dolomitization and associated mineralization. American Journal of Science **311**(7), 573–607 (2011) https://doi.org/10.2475/07.2011.01

Newman, J., Mitra, G.: Fluid-influenced deformation and recrystallization of dolomite at low temperatures along a natural fault zone, Mountain City window, Tennessee. GSA Bulletin **106**(10), 1267–1280 (1994) https://doi.org/10.1130/0016-7606(1994)106⟨1267:FIDARO⟩2.3.CO;2

Nakouzi, E., Steinbock, O.: Self-organization in precipitation reactions far from the equilibrium. Science Advances **2**(8), 1601144 (2016) https://doi.org/10.1126/sciadv.1601144

Ortoleva, P., Merino, E., Moore, C., Chadam, J.: Geochemical self-organization I; reaction-transport feedbacks and modeling approach. American Journal of Science **287**(10), 979–1007 (1987) https://doi.org/10.2475/ajs.287.10.979

Ortoleva, P.: Macroscopic self-organization at geological and other first-order phase transitions. In: Vidal, C., Pacault, A. (eds.) Non-Equilibrium Dynamics in Chemical Systems, pp. 262–274. Springer, Berlin, Heidelberg (1984). https://doi.org/10.1007/978-3-642-70196-2_14

Pillans, B.: Zebra rock – Australia's national rock. Blog post. Accessed: 2026-07-28 (2021). https://nationalrockgarden.com.au/featured-article/zebra-rock-australias-national-rock/

Palinkaš, S.S., Spangenberg, J.E., Palinkaš, L.A.: Organic and inorganic geochemistry of Ljubija siderite deposits, NW Bosnia and Herzegovina. Mineralium Deposita **44**, 893–913 (2009) https://doi.org/10.1007/s00126-009-0249-z

Passchier, C.W., Trouw, R.A.J.: Shear zones. In: Microtectonics, pp. 177–215. Springer, Berlin, Heidelberg (2005). https://doi.org/10.1007/3-540-29359-0_5

Putnis, A.: Mineral replacement reactions: from macroscopic observations to microscopic mechanisms. Mineralogical Magazine **66**(5), 689–708 (2002) https://doi.org/10.1180/0026461026650056

Retallack, G.J.: Zebra rock and other Ediacaran paleosols from Western Australia. Australian Journal of Earth Sciences **68**(4), 532–556 (2021) https://doi.org/10.1080/08120099.2020.1820574

Rye, R.O.: A review of the stable-isotope geochemistry of sulfate minerals in selected igneous environments and related hydrothermal systems. Chemical Geology **215**(1–4), 5–36 (2005) https://doi.org/10.1016/j.chemgeo.2004.06.034

Spear, F.S.: Metamorphic phase equilibria and pressure–temperature–time paths. Mineralogical Society of America Monograph., 352 (1993)

Saha, B., Roy, M.K.: Pattern formation and stability analysis in a fractional Gierer–Meinhardt model for metamorphic textures. Discover Geoscience **4**, 53 (2026) https://doi.org/10.1007/s44288-026-00425-5

Saha, B., Roy, M.K., Sarkar, B.K., *et al.*: Diffusion-driven orbicular dynamics of metamorphic granites. Journal of Earth System Science **134**, 192 (2025) https://doi.org/10.1007/s12040-025-02656-5

Sadek, S., Sultan, R.: Liesegang patterns in nature: A diverse scenery across the sciences, a review paper. In: Precipitation Patterns in Reaction-Diffusion Systems, pp. 1–43. Research Signpost, Trivandrum, India (2011)

Tompkins, L.A., Rayner, M.J., Groves, D.I., Roche, M.T.: Evaporites; in situ sulfur source for rhythmically banded ore in the Cadjebut Mississippi Valley-type Zn-Pb deposit, Western Australia. Economic Geology **89**(3), 467–492 (1994) https://doi.org/10.2113/gsecongeo.89.3.467

Taylor, A., Tinsley, M.: A path to patterns. Nature Chemistry **1**, 340–341 (2009) https://doi.org/10.1038/nchem.310

Vernon, R.H.: A Practical Guide to Rock Microstructure. Cambridge University Press, Cambridge (2004). https://doi.org/10.1017/CBO9780511807206

Watson, E.B., Baxter, E.F.: Diffusion in solid-Earth systems. Earth and Planetary Science Letters **253**(3–4), 307–327 (2007) https://doi.org/10.1016/j.epsl.2006.11.015

Wallace, M.W., Both, R.A., Morales Ruano, S., Fenoll Hach-Ali, P., Lees, T.: Zebra textures from carbonate-hosted sulfide deposits; sheet cavity networks produced by fracture and solution enlargement. Economic Geology **89**(5), 1183–1191 (1994) https://doi.org/10.2113/gsecongeo.89.5.1183

Wang, Y., Chan, M., Merino, E.: Self-organized iron-oxide cementation geometry as an indicator of paleo-flows. Scientific Reports **5**, 10792 (2015) https://doi.org/10.1038/srep10792

Yoshida, H., Katsuta, N., Sirono, S., Nishimoto, S., Kawahara, H., Metcalfe, R.: Concentric Fe-oxyhydroxide bands in dacite cobbles: Rates of buffering chemical reactions. Chemical Geology **552**, 119786 (2020) https://doi.org/10.1016/j.chemgeo.2020.119786

Yatsuda, Y., Tsushima, K., Fang, Q., Nabika, H.: Chemical model for pattern formation in rocks via periodic precipitation of iron oxide minerals. ACS Earth and Space Chemistry **7**(10), 2042–2049 (2023) https://doi.org/10.1021/acsearthspacechem.3c00165